FORCE SENSING INTEGRATED TIP AND ACTIVE READOUT STRUCTURES WITH IMPROVED DYNAMICS AND DETECTION RANGE

A Thesis
Presented to
The Academic Faculty

by

Byron Van Gorp

In Partial Fulfillment
of the Requirements for the Degree
Masters of Science Mechanical Engineering in the
School of Mechanical Engineering

Georgia Institute of Technology
May 2007

FORCE SENSING INTEGRATED TIP AND ACTIVE READOUT STRUCTURES WITH IMPROVED DYNAMICS AND DETECTION RANGE

Approved by:

Dr. Levent Degertekin, Advisor
School of Mechanical Engineering
Georgia Institute of Technology

Dr. Wayne Whiteman, Co-Advisor
School of Mechanical Engineering
Georgia Institute of Technology

Dr. Peter Hesketh
School of Mechanical Engineering
Georgia Institute of Technology

Date Approved: 4/9/2007

ACKNOWLEDGEMENTS

I wish to thank my fellow lab members for their help, Dr. Degertekin for giving me the opportunity to perform the research described in this thesis, and my family for supporting me throughout my research.

TABLE OF CONTENTS

Page

LIST OF TABLES

Page

LIST OF FIGURES

Page

LIST OF SYMBOLS

α_{step}	Relative Step Height in Membrane Due to Etch
b	Damping Coefficient
β	Residual Stress Term
$(\beta_n l)^2$	Eigenvalue Solution to Natural Frequency Equation
C_S	Sensitivity on Substrate
C_T	Total Sensitivity of Cantilever on Device
d	Distance from Grating to Reflector
d_c	Actuation Range Before Collapse
d_e	Phase Shift Etch Depth
D_k	Non-Dimensional Stiffness Coefficient
E	Elastic Modulus
ε_0	Permittivity of Air
ε_{Rox}	Relative Permittivity of Oxide
f_n	Natural Frequency in Hz
g	Gap Thickness
h_0	Effective Gap
I	First Moment of Beam
I_{in}	Laser Intensity Input
I_0	0^{th} Order Intensity
I_1	1^{st} Order Intensity
I_{ACnorm}	Measured AC Amplitude of 1^{st} Order Intensity

k	Bridge Device Theoretical Stiffness
K	Experimental Stiffness
κ	Rotational Elastic Stiffness Coefficient
K_C	Calibrated Cantilever Stiffness
K_{eff}	Effective Stiffness
k_{mem}	Stiffness of Circular Device
k_{rt}	Stiffness of Beam with Uniform Rotational Elastic Support
K_{ref}	Stiffness of Reference Cantilever
L	Bridge Length
L_e	Electrode Length
λ^2	Eigenvalues of Plate Problem
λ	Wavelength of Laser
m_{eff}	Effective Mass
μ	Viscosity of Air
ω_P	System Natural Frequency
ω_n	Bridge Natural Frequency
P_0	Pressure of Air
p_o	Dynamic Response Transfer Function Parameter
ϕ	Optical Path Length Shift
$\phi(x)$	Mode Shape
Q	Quality Factor
ρ	Density of Device
σ	Film Intrinsic Stress
t	Thickness of Bridge

t_{ox}	Thickness of Oxide
ϑ	Angle of Cantilever Tip
U	Uncertainty of Sensitivity Measurement
U_K	Uncertainty of Stiffness Measurement
V_c	Collapse Voltage
ν	Poisson's Ratio

LIST OF ABBREVIATIONS

AFM	Atomic Force Microscope
ANSYS	ANSYS Finite Element Software
FEM	Finite Element Model
FIRAT	Force Sensing Integrated Tip and Active Readout
He-Ne	Helium-Neon
PD	Photo Detector
PECVD	Plasma Enhanced Chemical Vapor Deposition
RIE	reactive ion etch
SEM	Scanning Electron Micrograph
TRIF	Time Resolved Interaction Force

SUMMARY

It was previously shown that a Force Sensing Integrated Tip and Active Readout Structure (FIRAT), with its integrated actuator and phase-sensitive diffraction grating, can feasibly obtain piconewton force resolution along with increased bandwidth. The advantages over cantilever based implementations have been developed, yet the FIRAT structure suffered from a limited interferometric displacement detection range of about quarter of the laser wavelength, its dynamics were dominated by squeeze film damping, and the stiffness was not suitable for some imaging applications. The limitation in range was inherent to the optical detection scheme used. Modifications to the previous structure design and sensor detection scheme are implemented in order to increase the detectable displacement range, improve dynamic response and stiffness, and custom tailor these devices for particular imaging applications.

A sensor structure is introduced, which uses phase shifted dual diffraction gratings in order to increase the detectable range of motion when using phase sensitive diffraction for optical interferometric detection of displacement in probe microscopy. The structure is based on a previous implementation of FIRAT sensor used in AFM imaging. With a new design and modified geometry/fabrication process, FIRAT structures with improved displacement detection range and dynamic response are demonstrated. Increased detection range is obtained by imparting a 90 degree phase shift, between optical output curves of the two integrated gratings. The phase shift is introduced via a micro-machined step in the quartz substrate below one of the gratings.

An increase in detectable motion of 4 times that of previous FIRAT structures is demonstrated via the modified fabrication process. Bridge shape devices were characterized, that possessed natural frequency ranging from 30 kHz to 1.2 MHz, with Q from 1 to 15 and stiffness ranging from 1 to 100 N/m. Actuation displacement range using the electrostatic actuator was increased 3 times, via the increased gap thickness. A theoretical model useful in design was verified to predicate the structures dynamic response, stiffness and detection scheme.

CHAPTER 1 :

BACKGROUND AND INTRODUCTION

1.1 AFM Background

The atomic force microscope has been a very useful instrument in a variety of research areas, and has become increasingly more useful since its inception in 1986 [1]. It allows the researcher to directly measure forces at the surface in the pico-newton range [2] and with AFM, experiments measuring topography can be performed on insulating and conducting surfaces. Being able to measure pico-newton order forces in nano-scale locality allows researchers to investigate interactions at the surface interface and image samples that cannot be scanned use other techniques. Some of its uses include, but are not limited to, quantitative material characterization, topography with nano-scale resolution, biological imaging and investigation of various surface science phenomenon [3]. Some of the major challenges in applying AFM are related to, uncertainties in tip shape and cantilever elastic modulus, gaining increased imaging speed and bandwidth via arrays or tips driven by integrated actuators; measuring Transient Interaction Forces [4] and interpreting Force-Displacement Curves.

The key components of an AFM imaging system are the tip, scanner / approach mechanisms, motion detector, and a computer for feedback control and imaging system. Figure 1 shows a typical schematic of an AFM device utilizing a cantilever and beam bounce detection for displacement sensing.

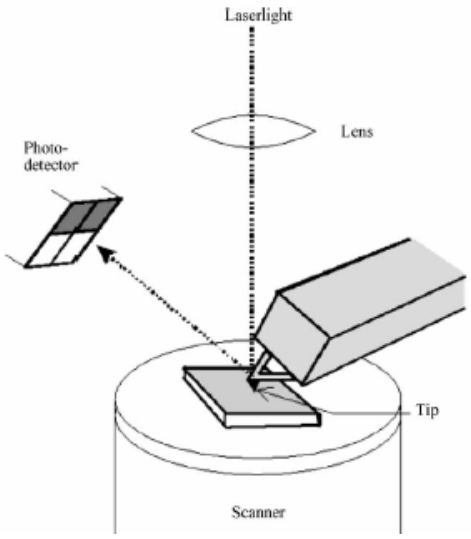

Figure 1: Typical Schematic AFM [3].

The optical beam bounce system consists of a laser that is reflected of the tip of the cantilever toward a split photodetector, and a scanner on which the sample being measured is attached to. Either the scanner or the holder is translated in the x, y, and z directions via piezoelectric actuators. The deflection of the beam is then obtained by relation to the movement of the reflected laser spot on the photodetector.

One of the key components of AFM is the motion sensor which detects displacement of the AFM tip allowing topography and interaction force data to be obtained. There are several displacement sensing schemes which have been implemented for this purpose including capacitive, piezoresistive [5] or optical detection. Examples of optical sensors include, laser beam deflection [6], homodyne [7] and heterodyne [8] interferometry, and laser diode feedback [9]. Laser beam deflection offers a simple way of measuring displacement, yet it is limited to cantilever type structures and slope detection. The detection sensitivity can be increased with an interferometrical approach [7]. Each of the optical detection techniques mentioned have their own advantages and

drawbacks, yet they share the common thread of utilizing a cantilever type structure and its accommodating actuation mechanism.

Disadvantages of cantilever based AFM include: slow actuation speed using conventional piezo stack, beam bounce detection being less sensitive than other interferometric methods, complex implementation for creating arrays, and high Q (quality factor of dynamic response) of cantilevers which may not be suitable for material properties imaging.

1.2 Previous Generation of FIRAT with Circular Membranes

An AFM sensor structure, with integrated actuator, that can feasibly obtain Pico-Newton force resolution along with increased bandwidth has been previously introduced [10]. Figure 2 shows a schematic of the FIRAT (Force sensing Integrated Tip and Active Readout) sensor structure.

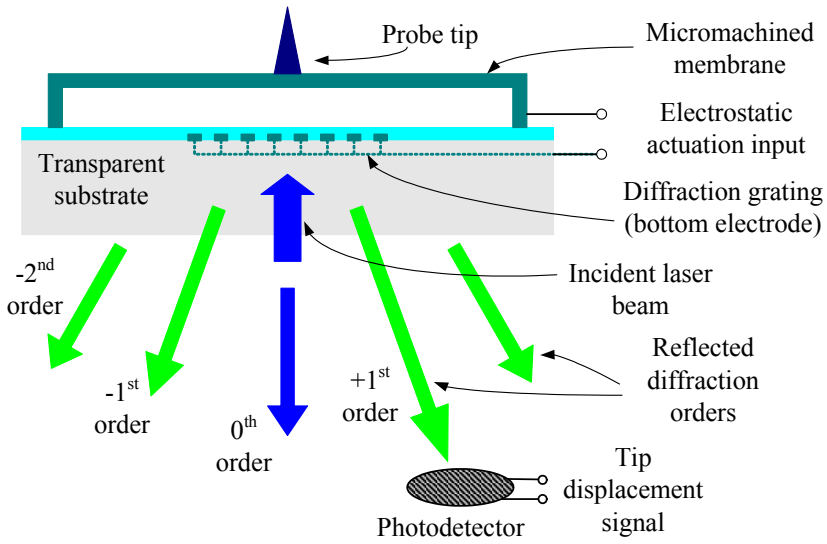

Figure 2: Schematic of FIRAT Sensor Structure [10].

With this structure, displacement sensitivity on the order of 2×10^{-4} Å/√Hz [4, 11, 12] can be obtained, and with the addition of a sharp tip, experiments were performed showing

its ability to directly measure transient interaction forces, perform material imaging and its suitability for fast tapping mode imaging [10]. The structure consists of a micromachined membrane that is fabricated upon a transparent substrate. A diffraction grating that also serves as a bottom electrode is located on the quartz substrate. The combination of the diffraction grating and bridge structure/reflector, serve as a phase sensitive diffraction grating [13, 14] and integrated electrostatic actuator. A coherent light source is focused on the grating and the resulting reflected diffraction orders are measured using a photodetector. The measured intensity from the photodetector serves as the tip displacement signal for AFM imaging. A sharp tip is mounted at the center of membrane to complete the probe structure. Figure 3 is a SEM image of a FIRAT circular membrane device, with metal sharp tip fabricated using FIB deposition.

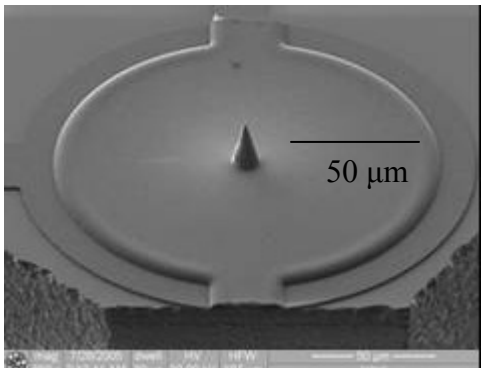

Figure 3: Circular FIRAT Membrane with FIB metal sharp tip [10]

The FIRAT structure has several advantages over a typical cantilever implementation using beam slope detection: the phase sensitive diffraction grating provides higher displacement detection sensitivity; it's integrated electrostatic actuator is better suited for fast imaging applications; and the geometry / detection scheme allow array structures to be easily fabricated. The advantages of the integrated phase-sensitive diffraction grating and electrostatic actuator over other cantilever based implementations

are well developed, yet the circular FIRAT structure suffers from limited displacement detection range of a quarter of a wavelength (167.5 nm for $\lambda = 670$ nm), also its dynamics were dominated by squeeze film damping and the stiffness was not suitable for many imaging applications. This limitation in detection range was inherent to the optical detection scheme used.

1.3 Motivation

Utilizing the FIRAT structure's integrated electrostatic actuator, the imaging speed of FIRAT structures is limited only by the device dynamics. The previous circular membrane devices were dominated by squeeze film damping due to the structure geometry. Air trapped between the membrane and the substrate caused a low frequency cutoff and spring stiffening at high frequencies. To utilize the FIRAT structure for fast imaging applications, a flat response across the entire bandwidth is desired. Figure 4 shows the dynamic response of a circular FIRAT membrane structure.

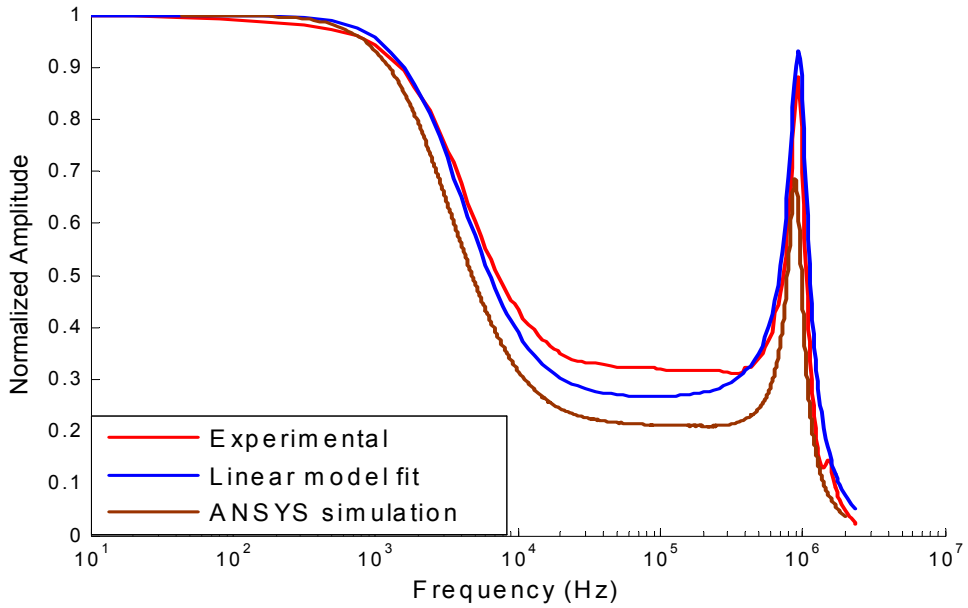

Figure 4: Circular FIRAT Membrane Dynamic Response [10].

The circular device has a low frequency cutoff at 1 kHz. Also, actuation range and stiffness was limited by geometry. By introducing larger gap devices, with bridge shaped geometry, devices can be fabricated with improved dynamic response and stiffness. The increase in gap height will reduce damping and increase actuation range.

Displacement detection range was limited to ¼ wavelength of the Laser, about 158 nm detection range (1/2 cycle of optical curve). The optical output varies sinusoidally with gap distance, and sensitivity becomes zero with every ½ cycle of the optical curve. The maximum displacement detection range is generated by the sensitivity decreasing to zero at the max/min points in the optical curve. The theoretical optical output curves for the 0^{th} and 1^{st} orders are given in Figure 5.

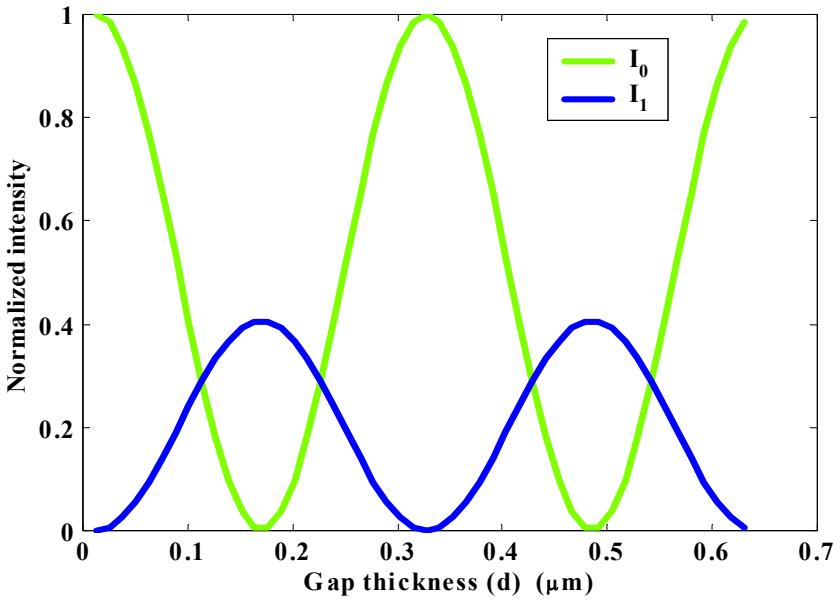

Figure 5: Circular FIRAT Membrane Optical Curve [10].

An increase in displacement sensor range is implemented by either increasing the period of the optical curve, so that sensitivity is constant throughout a longer displacement

range, or by utilizing phase shifted dual gratings to readout two optical outputs. A desired 90 degree phase shift, between optical output curves of two integrated gratings, can be introduced via a micro-machined step in the quartz substrate below one of the gratings. The concept is shown by measuring the optical output of each grating while displacing the bridge both via electrostatic actuation. Both gratings can be used together in order to increase the range of displacement detection beyond that of previous implementations of this sensor type.

1.4 Metrics and Design Requirements of Force Sensing Structures

Utilizing a FIRAT circular membrane structure transient interaction forces have been directly measured for use in material imaging [10]. TRIF mode is similar to tapping mode with a cantilever, yet force versus displacement data is acquired with each contact of the tip with the surface. Requirements are high sensitivity of AC signal measurement, and stiffness from 1 to 30 N/m is desirable. Structures that are not very high Q, over damped or subject to low-frequency cut-off from squeeze film damping are necessary.

There are several important factors that affect a probe's suitability for Fast Imaging. First, the dynamic response must be tailored toward imaging experiments at high speeds. This demands a flat frequency response with a relatively high resonance frequency, preferably in the MHz range. A stiffness of 10-40 N/m is suitable for high speed imaging experiments. The structure’s overall force noise throughout the useable imaging bandwidth should be minimized, and frequency dependent forces due to squeeze film damping should be eliminated if possible. The device should possess low damping and have Q on the order of 10 – 50, and if possibly higher. An actuation range of 1 μm or larger is desirable.

Experiments utilizing these structures are performed on retrofitted commercial AFM systems. It has an integrated diode laser and photodetector. The orders need to be spaced far enough apart so that a single reflected order can be measured on the photo detector. A 4 μm period proved very suitable the previous generation of circular membranes. The spot size of laser, focused on the grating, must be a large enough to cover several grating periods, but small enough to focus on the flat moving section of a bridge structure. Because the spot size is fixed by the diode laser and accompanying optics, the device must be wide enough to collect most of the laser spot. Widths around 80 μm or larger are most suitable, yet optical detection may be possible down to 20 μm wide.

The motivation for the new design of FIRAT devices is to provide force sensing structures that are better suited for AFM imaging. Table 1 shows the List of Metrics and their relation toward fulfilling design requirements.

Table 1: Table of Metrics

#	Metric	Description	Units	Fast - Imaging Target	Tapping / TRIF	Extended Range
1	Collapse Voltage	Voltage at which device becomes ustable and collapses. Relates to actuation voltage.	Volts	< 300	< 300	< 300
2	Actuation Range	Range of displacement under electrostatic actuation before collapse.	μm	> 1	> 1	> 2
3	Natural Frequency	Natural frequency of the structure's first mode shape.	kHz	> 1000	> 100	> 100
4	Bandwidth	Range of frequency response with flat response.	kHz	800	60	60
7	Quality Factor	Quality Factor. Relates to energy loss and damping of system.	N/A	10 - 100	< 3	>1
8	Stiffness	Stiffness of the sensor to point loading at center of bridge.	N/m	10 - 40	1 - 30	10 - 40
9	Modulation Depth	(Max optical signal - Min optical Signal) / Max optical signal. Relates to optical losses	%	> 60	> 80	> 80
11	Displacement Sensor Range	Maximum displacement dectection of optical motion sensor.	nm	150	150	1000

Metrics must be developed so that designs can be evaluated for suitability and satisfaction of requirements. The important operating characteristics and design considerations discussed previously were analyzed in creating this set of metrics. Table 2 shows a summary of the resulting requirements for the FIRAT structure design.

Table 2: Requirements List

MIST GROUP		**Requirements List for the Design and Fabrication of Force Sensing Structures for AFM Imaging**
Problem Statement: Design force sensing structures that can be used for a wide range of imaging applications and are easily integrated into a commercial AFM system.		
#	**Demand/Wish**	**Requirements**
General Requirements		
1	W	Utilize previous fabrication techniques and design knowledge
2	D	Develop design that provides scalability toward next generation
3	W	Utilize other group members knowledge and experience
Specific Requirements		
4	D	Develop Design Suitable for Several Target Imaging
5	D	Fast Imaging / Arrays
6	D	Tapping Mode and TRIF
7	D	Contact Mode / Static Force-Displacement
8	W	Friction Experiments
9	D	Increased Range Devices
10	D	Develop design suitable for implementation in commercial
11	D	Develop theoretical model that facilitates design of target
12	D	Develop characterization method that aids in verification of
13	D	Develop modified fabrication process needed to satisfy

CHAPTER 2 :

FABRICATION OF FIRAT DEVICES

2.1 Process Flow and Fabrication

The 3rd generation process flow was originally developed for optical capacitive micromachined ultrasonic transducers [15]. By adding a sharp tip to these circular membranes they can be used for AFM imaging. Improved dynamics and increased operation range are obtained through several modifications: a large gap sacrificial layer for reduced squeeze film damping, recessed gratings for oxide-less (passivation layer) devices, and use of new masks with bridge structures. Figure 6 below shows the process flow for the fabrication.

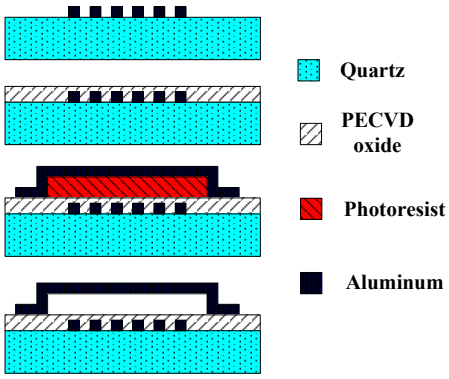

Figure 6: Process Flow Diagram[15].

Optical lithography is used to pattern a sacrificial layer for the 4 μm period diffraction grating, which is metallurized using an E-beam evaporator. By using a standard lift-off process leaves only the patterned grating. Subsequently, an insulating layer of PECVD oxide is deposited upon the quartz, isolating the fingers from the top electrode. The aluminum bond pads connecting to the gratings are opened by patterning a photoresist

mask and then etch in with a reactive ion etch (RIE). The sacrificial layer is then patterned with a desired thickness to determine the device gap height. The desired thickness top electrode/bridge is deposited using aluminum with 1% Si from a DC sputterer at 40% power. The planar shape of the devices is then patterned with a photoresist mask and etched using wet aluminum etchant (Type A).

2.1.1 Electrode/Optical Grating Patterning and Lift Off

Since a lift off process was used (60 degrees Celsius, Acetone 0.5 hrs, ultrasonic bath 60 sec), the spacing between the fingers is very dependent on the Shipley Coatings 1813 photoresist that is patterned before metallization. If the resist is exposed or developed for too long the aluminum fingers will be wider than the slits between the grating fingers. For max optical modulation, the size of fingers and opening should be equal. Since the period of the grating is 4 μm, each should be 2 μm. This can be achieved relatively accurately with optimal lithography settings. Figure 7 shows a picture of an example grating after lift off.

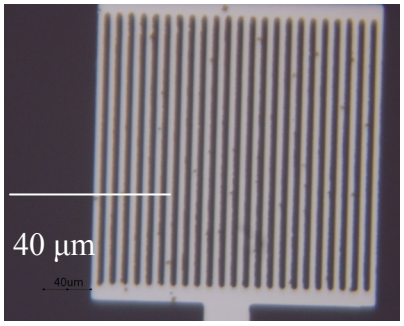

Figure 7: Micrograph of 2 μm Period Grating after Lift Off.

The above grating was fabricated using a 10 nm of Ti for adhesion and 100 nm of aluminum, because of its desirable optical properties. If the adhesion layer is less than around 30 nm, the reflectively of the aluminum grating is not affected substantially.

In order to eliminate the necessity for the oxide passivation layer, the first process step can be modified so that the metal grating/electrode is just below the surface of the quartz substrate. The patterning of the photoresist is performed as originally, but before depositing aluminum for the grating, the exposed quartz is etched a depth just larger than the thickness of the grating. Figure 8 shows a surface plot of an example recessed grating using an optical prolifometer.

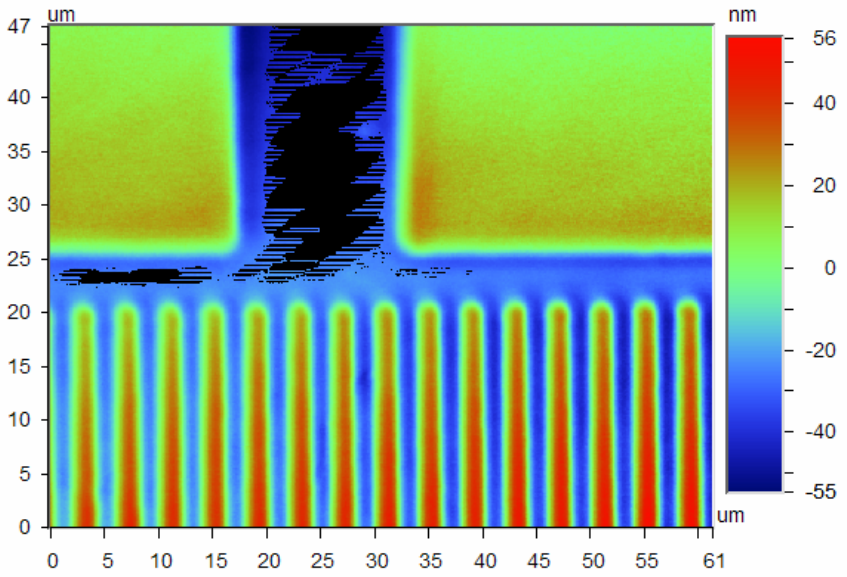

Figure 8: Prolifometer Cross Section of Embedded Grating.

The 110nm grating is recessed in a 120nm trench that serves to isolate it from the top electrode during collapse under electrostatic loading.

2.1.2 Passivation Layer (Oxide) Deposition

A passivation layer of Plasma Enhanced Chemical Vapor Deposition (PECVD) oxide (at 250 degrees Celsius process temperature) is used to protect the device during collapse as discussed above. 200 nm of oxide are deposited in order to prove complete coverage of the grating structure. After deposition a photoresist mask is patterned using

SC 1827, leaving only desired portions of the bottom electrode bond pads open. The oxide layer above the aluminum bond pad is etched using a Reactive ion etch (RIE), with the standard oxide process. A refractometer is used to measure thickness of the oxide layer and insure complete removal of oxide on the bond pad.

2.1.3 Sacrificial Layer Patterning and Bridge Structure Deposition

The bridge gap affects the dynamic response of the structures greatly. It can be adjusted through use of different photoresists to make up the sacrificial layer. Also the thickness of each resist can be adjusted through modification of its application variables, namely the spincasting parameters. The previous generation of devices used a photoresist that was limited to around 3 μm height using our procedures. This is a suitable gap for tapping and contact devices where high Q and bandwidth are not necessarily needed. For fast imaging and TRIF experiments it is desirable that the dynamic response is not dominated by squeeze film damping. For this reason a process was developed utilizing resist that can range from 4 to 8 μm in height. Figure 9 shows a picture of the photoresist sacrificial layer after development.

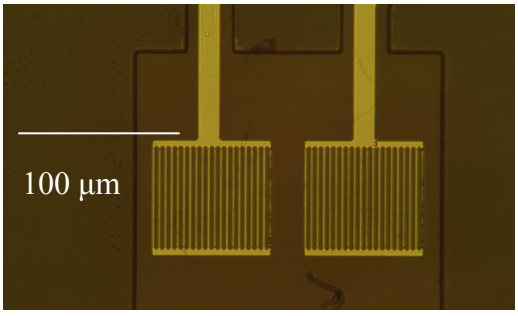

Figure 9: Micrograph Image of 4.5 μm Photoresist Sacrificial Layer.

The sidewall slope and profile of the sacrificial layer is very important to fabrication and also the optical detection scheme. The surface of the bridge must be relatively smooth so

that the laser beam is reflected back normal to its surface. If there are ripples or steps in the surface, the phase sensitive detection scheme will suffer. A sufficient post bake of the sacrificial layer will tend to smooth out any roughness due to the grating or substrate below the surface of the resist. This also induces an edge bead to form at the perimeter of the sacrificial layer. The edge bead is visible in Figure 10, a prolifometer scan of patterned 5.0 μm thick resist.

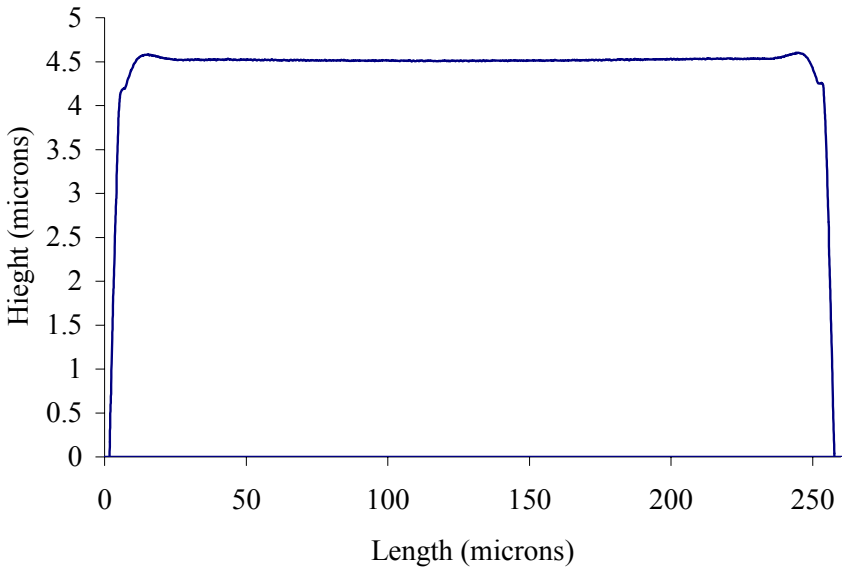

Figure 10: Prolifometer Scan of 5 μm Photoresist Sacrificial Layer

Also it is notable that there is a significant side wall slope at the edge of the sacrificial layer. This is a desirable because, although the sputtered aluminum film that makes up the bridge structure is conformal, the sidewall coverage decreases as the aspect ration goes up and uniformity other film thickness therefore occurs at these locations. The sidewall slope can be increased by adjusting the exposure time during patterning of the resist layer. The thicknesses deposited, ranged from 0.5 to 1.01 μm as measured with an AFM using a 0.1 N/m contact cantilever.

The stress of the aluminum film that is sputtered on top of the sacrificial layer can be characterized using a prolifometer. The stress was estimated by measuring the wafer curvature, with a prolifometer, before and after deposition of aluminum to be around 8 MPa compressive. The stress was calculated by treating it as a thin film on top of a much thicker substrate. The accuracy of the stress calculation, for that low magnitude of a stress measurement, is not very good, yet the fact that it is compressive is verified as the released devices were bowed up. Since the devices have bridge geometry, a compressive stress will result in a bowed up structure and tensile in a bowed down structure.

2.1.4 Etch Mask Patterning and Wet Etch of Bridge Layer

The etch mask patterning is a very crucial step in fabrication of large gap devices. The resist layer below is very sensitive to temperature and will out gas if heated too much during the following process steps. This was a problem during initial processing of large structures. The fabrication would proceed fine until the first soft bake of the etch mask photoresist layer. At that step, the aluminum, that covers the entire wafer before etching, would bubble up in areas where the sacrificial layer was present. By increasing the soft and hard bake times and lowering temperature of the etch mask (6 min at 90 degrees Celsius), a process was found that prevented out gas of the sacrificial layer, yet still maintained reasonable resolution of the etch mask and bridge patterning. The sacrificial layer was most likely out-gassing moisture that was not completely baked out during hard bake or trapped on the surface before deposition of the sputtered aluminum.

The previous fabrication technique used a 2 μm thick photoresist etch mask to pattern the circular membranes. During spin casting the large gap devices provide a significant obstacle to conformably cover using only a 2 μm thick etch mask. This

resulted in uneven coverage on one side of the bridge, and during wet etch that end was substantially damaged, resulting in device failure. By using a 4.5 to 5 μm resist layer as the etch mask, this problem was averted. Figure 11 shows a micrograph of a 60 x 20 μm bridge after patterning and wet etch of the top aluminum layer.

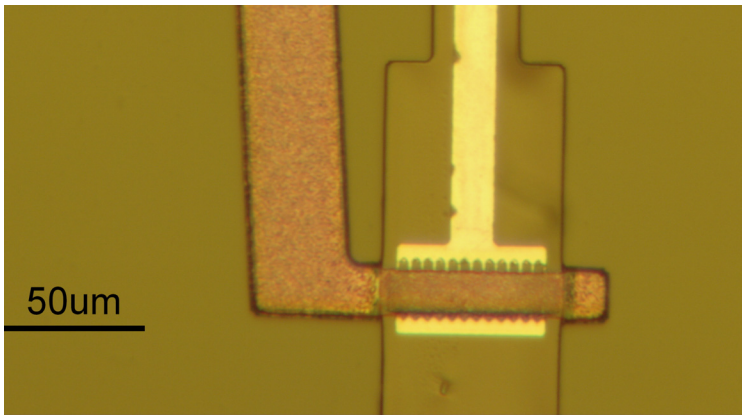

Figure 11: Micrograph of Etch Mask Wet Etched 60x20 μm Bridge.

It is evident, as described earlier, that the left hand side of the bridge has excessive sidewall etching which damaged this device. Figure 12 shows a released 5 μm gap device that was etched successfully.

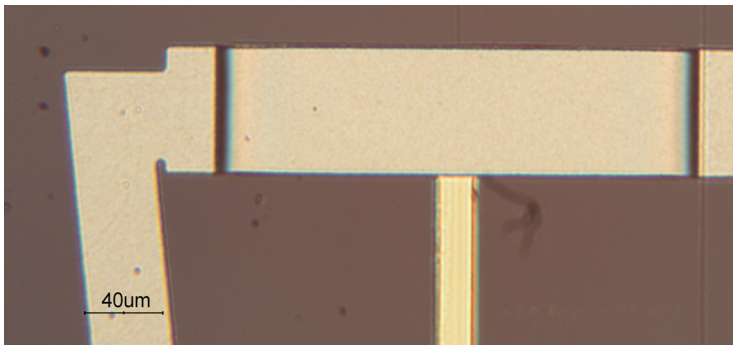

Figure 12: Micrograph of Released Bridge Device.

The finished bridge devices are released, after the chips are diced to proper size and geometry for either testing or imaging, by submersing in acetone to dissolve the sacrificial layer away. Structures with stiffness ranging from 1 to 100 N/m, as measured

with a calibrated AFM cantilever, were fabricated. The main cause of failure during release is the bridge collapsing under the meniscus force as the isopropyl alcohol evaporates out of the gap between bridge and substrate. Some of these devices were easier to release than others because of geometry (length/gap) and stiffness. Devices that were very soft or large were released in a critical point dryer to avert this problem. It was found that devices of length less than 100 μm could be wet released with reasonable yield (around 80% of devices released without collapsing).

CHAPTER 3 :

THEORETICAL AND COMPUTATIONAL MODELING

3.1 Theoretical Models

3.1.1 Beam/Membrane Stiffness

A force sensing structure, used for Atomic Force Microscopy, must be tailored to suit its application. If the probe is too stiff and the sample being measured is relatively soft, the sample may be damaged during imaging. For example, the stiffness of AFM cantilevers can range anywhere from 0.001 N/m to 100 N/m, depending on the application. The basic geometry utilized in fabrication of the FIRAT devices is a bridge structure, depicted in Figure 13.

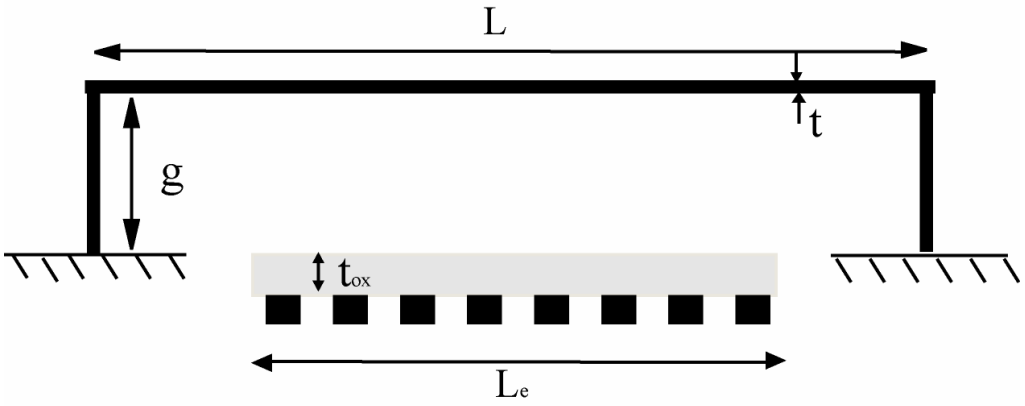

Figure 13: Diagram of Typical Bridge Structure.

The bridge device can be modeled as a clamp-clamp beam that is point loaded at the center of the beam. The stiffness for a clamp-clamp beam assuming small deflections and no shear effects is given by Equation 3.1 [16],

$$k_{cc} = 16Ew\left(\frac{t}{L}\right)^3 \qquad (3.1)$$

where k is stiffness, E is modulus of elasticity, h is the thickness of the beam and L is the length of the beam.

Some large gap structures may have sidewalls that are significantly large in proportion to the length. For these devices the assumption of clamped boundary conditions may not be valid. This case is modeled by replacing the clamped conditions with uniform rotational elastic boundary conditions. The rotational elastic stiffness constant, κ, can be estimated by a frame analysis of the bridge structure to be EI/g. This is done by treating the side wall as a clamped beam with a moment applied at its end [16]. The stiffness constant is found by equating the moment to a rotation at the beam tip, multiplied by the stiffness constant. Using the method of superposition the beam equation can be solved similarly to a clamped beam, but with mixed boundary conditions. The resulting stiffness for a point load is given by Equation 3.2 below.

$$k_{rt} = 16Ew\left(\frac{t}{L}\right)^3 \frac{\left(1+\frac{\kappa L}{2EI}\right)}{\left(4+\frac{\kappa L}{2EI}\right)} = 16Ew\left(\frac{t}{L}\right)^3 \frac{\left(1+\frac{L}{2g}\right)}{\left(4+\frac{L}{2g}\right)} \qquad (3.2)$$

Since devices will be fabricated with L/w aspect ratios ranging from 1 to 5, the geometry should not be treated as a narrow beam. Therefore, E, in Equation 3.1 and 3.2, above should be replaced by the plate modulus, $E/(1-v^2)$ [17].

3.1.2 Natural Frequency and Mode Shapes

The natural frequency of a clamped-clamped beam is given by the following Equation 3.3 [17].

$$f_n = \frac{(\beta_n l)^2}{2\pi}\sqrt{\frac{E}{12\rho(1-v^2)}}\frac{t}{L^2} \qquad (3.3)$$

where ρ is the density, and $(\beta_n l)^2$ is the eigenvalue, or solution of the natural frequency equation. Note that the plate modulus is used as the aspect ratio *L/w* less than 5. For a clamped end beam condition, assuming no shear affects and small deflections, $(\beta_n l)^2$ is found by solving Equation 3.4.

$$1-\cosh(\beta_n l)*\cos(\beta_n l)=0 \qquad (3.4)$$

Solutions to Equation 3.4 are readily available, with the first root being approximately 4.73.

By adding similar mixed boundary conditions as prescribed for the stiffness analysis on large gap devices, the effect of the compliant edge conditions is approximated. Again the beam is modeled as a having uniform rotational elastic boundary conditions given by Equation 3.5.

$$\begin{aligned} &y(0,t)=0 \\ &EI\frac{\partial^2 y(0,t)}{\partial x^2}=\kappa\frac{\partial y(0,t)}{\partial x} \end{aligned} \qquad (3.5)$$

Using similar technique as [17], the natural frequency equation for uniform rotational elastic boundary conditions is derived and given by Equation 3.6

$$\begin{aligned} &1-\cosh(\beta_n l)*\cos(\beta_n l)+2*\left(\frac{EI}{\kappa L}\right)^2(\beta_n l)^2\sinh(\beta_n l)*\sin(\beta_n l)=0 \\ &\kappa=\frac{EI}{g}\Rightarrow 1-\cosh(\beta_n l)*\cos(\beta_n l)+2*\left(\frac{g}{L}\right)^2(\beta_n l)^2\sinh(\beta_n l)*\sin(\beta_n l)=0 \end{aligned} \qquad (3.6)$$

Note the substitution of *EI/g*, in for the uniform rotational elastic spring constant as explained in the previous section. This equation can be solved numerically given a value

for *g/L*. As *g/L* approaches zero, the solution converges to 4.73 that of the clamped case, and as *g/L* approaches infinity the solution converges to ~ 3.15, that of the pinned case.

The mode shape, $\phi(x)$, for the clamped-clamped beam is given by Equation 3.7 [17],

$$\phi(x) = \frac{\cosh\left(\frac{\beta_n l}{L}x\right) * \cos\left(\frac{\beta_n l}{2}\right) - \cos\left(\frac{\beta_n l}{L}x\right) * \cosh\left(\frac{\beta_n l}{2}\right)}{\cosh\left(\frac{\beta_n l}{2}\right) - \cos\left(\frac{\beta_n l}{2}\right)} \qquad (3.7)$$

Figure 14 shows a plot of the first three flexural modes versus normalized length, *x/L*.

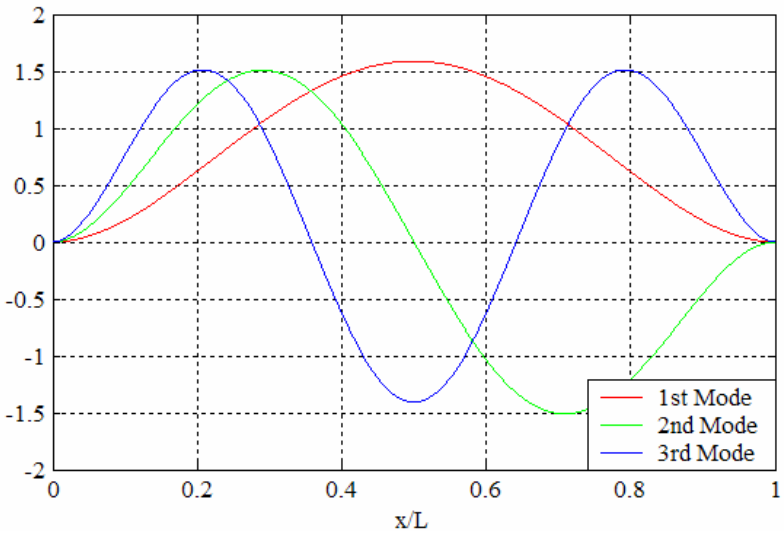

Figure 14: Mode shape of 1st, 2nd and 3rd modes of clamped beam.

The mode shape is important because of several reasons. Depending on what mode is being excited the laser spot and grating may or may not be centered over a relatively flat area. Also for friction experiments, the fact that the 2nd mode has a node point in the center of the bridge will be used.

For plates with aspect ratio, *L/w*, near unity the eigenvalues will be dependent on the aspect ratio, and edge conditions if modeled with compliant boundary conditions.

Utilizing building blocks similar to that of Clamped-Free-Clamped-Free plate [18], and adding the required constraints so that the boundary conditions are uniform rotational elastic support instead of clamped, the eigenvalue matrix is generated using the code given in Appendix B. $(\beta_n l)^2$ in Equation 3.3 is replaced by $\lambda^2 = f(L/w, \kappa, poissons)$, where as before κ is the edge rotational stiffness coefficient is equal to *L/g*. The plate problem is simplified using symmetry, analyzing only a ¼ section of the plate. The 1st mode eigenvalues were calculated for a typical range of values of *L/w* and *L/g*. Figure 15 is a contour plot of eigenvalues versus the aspect ratios. Note that the theoretical value of $(\beta_n l)^2$ for the Clamped beam is 22.37.

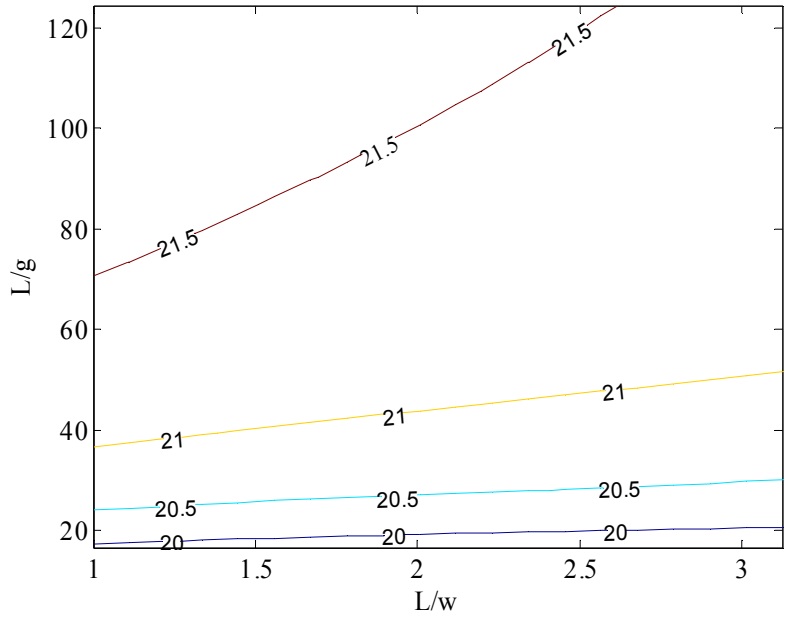

Figure 15: Eigenvalues of Plate with Rotational Elastic Support.

Although the eigenvalues vary dependently upon gap and width aspect ratios, the change from the clamped theory is at most 10 % difference. For devices with small gaps and relatively large lengths the clamped theory will most likely overestimate, yet be close to

the actual value. Devices with aspect ratios close to unity and large gaps however should be calculated using the plate theory. Figure 16 shows a calculated mode shape.

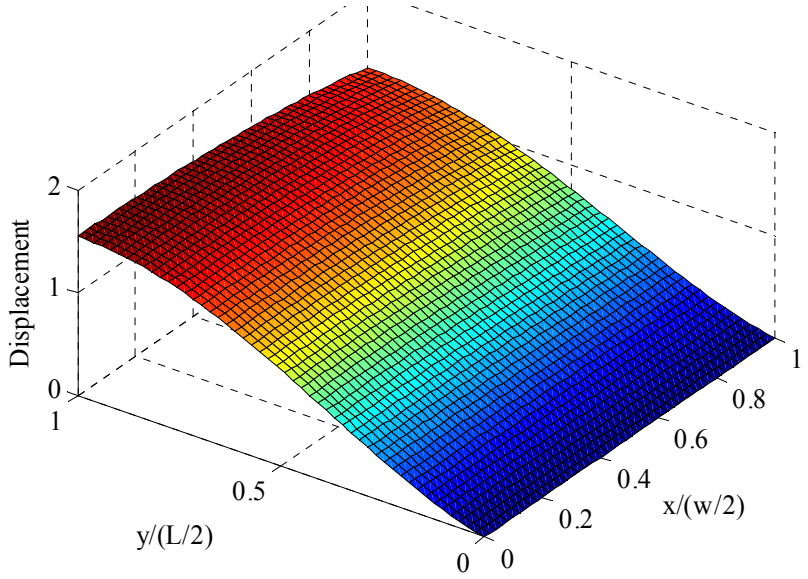

Figure 16: Mode Shape of ¼ Section Beam with *L/w*=1 and *L/g*=10.

The mode shape for the ¼ section of the beam is easily calculated once the eigenvalue matrix has been created. One can also use superposition of the mode shapes to calculate the stiffness for a point load.

3.1.3 Dynamic Response and Squeeze Film Damping

The dynamic response of the structure is very important to the imaging application because it affects the force applied to the sample, the imaging speed, and other aspects. Because the air gap, *g*, between the bridge structure (top electrode) and the substrate is on the order of 2 μm, squeeze film damping is not negligible. A lumped mass model can be used to model the dynamics of the system for design purposes. The transfer function for the system is given by Equation 3.8 [19],

$$G(s) = \frac{\omega_n^2 (s + \omega_c)}{s^3 + \omega_c s^2 + (\omega_c \frac{b}{m_{eff}} + \omega_n^2) s + \omega_n^2 \omega_c} \quad (3.8)$$

where $\omega_n = 2\pi f_n$ is natural frequency in radians/s, b is the damping constant, m_{eff} is the effective mass, and ω_c is the cutoff frequency. The effective mass can be estimated by integrating the norm of the mode shape, and is given by Equation 3.9 [20],

$$m_{eff} = \int_{-L/2}^{L/2} \rho w t \phi^2(x) dx \quad (3.9)$$

where ρ is mass density. For the first mode shape the effective mass is equal to approximately $0.3965 \rho wtL$. The damping coefficient and cutoff frequency are given by Equations 3.10 and 3.11, respectively [19],

$$b = \frac{96 \mu L w^3}{\pi^4 g^3} \quad (3.10)$$

$$\omega_c = \frac{\pi^2 P_0 g^2}{12 \upsilon w^2} \quad (3.11)$$

where μ is the viscosity, and P_0 is the pressure. The response transfer function can be rewritten as a factored 3rd order system as in Equation 3.12

$$G(s) = \frac{(s + \omega_c)}{(s + p_o)(s^2 + \frac{\omega_P}{Q} s + \omega_P^2)} \quad (3.12)$$

where Q is the quality factor, ω_P is the damped systems natural frequency, and p_o is the low cutoff corner frequency. ω_P, p_o, and Q can be solve for by equating terms in Equations 3.8 and 3.12. By analyzing the frequency response of the previous system, the resonance frequency, damping, and other important information are found, such as

whether the system is afflicted by a low frequency cutoff or squeeze film spring stiffening.

3.1.4 Collapse Voltage

The collapse voltage is the voltage at which the bridge becomes unstable under electrostatic load, and collapses from the min gap distance to direct contact with the substrate. It is important because the imaging controller must be designed to handle the correct actuation voltage. Huang [20] suggests a model for the collapse voltage of a rectangular bridge shaped device of length L, with a bottom electrode of length L_e, as shown in Figure 13. The effective stiffness constant K_{eff}, is the stiffness at the center of a beam under partially uniform distributed load, and is given by Equation 3.13

$$K_{eff} = \frac{32Et^3}{L_e(2L^3 - 2L_eL^2 + L_e^2)} + \frac{8\sigma t}{2LL_e - L_e^2} \qquad (3.13)$$

where σ is the axial stress. The above equation assumes a small residual stress term, β, given by Equation 3.14

$$\beta = \frac{L}{2t^2}\sqrt{\frac{12\sigma}{E}} \qquad (3.14)$$

The stress becomes very important as the thickness of the beam decreases and length increases. This will be apparent in the fabricated structures. The critical collapse voltage, V_c, is given by Equation 3.15

$$V_c = \sqrt{\frac{8K_{eff}h_o^3}{27\varepsilon_0[1 + 0.42(h_0 / w)]}} \qquad (3.15)$$

where ε_0 is the permittivity of air and the effective gap, $h_0=g+t_{ox}/\varepsilon_{Rox}$. ε_{Rox} is the relative permittivity of the oxide (3.9). The actuation range is the distance the bridge can be actuated before collapsing, $d_c = g - 2/3h_0$.

3.2 ANSYS Computational Modeling

A 3D ANSYS finite element model was created to assess the stiffness and natural frequency of bridge devices, under approximated point loading, with *L/w* aspect ratios approaching unity. Symmetry was used and the bridge structure was modeled as a ¼ section. Structural loading analysis was performed using Solid45 elements to calculate the structures stiffness, and a subspace solver was used to calculate the first three mode shapes. Asymmetry was used across the beams center (width direction) axis in order find the 2nd mode shape for use in friction tapping. Figure 17 below shows the 2nd mode shape, or the first fully Asymmetric mode.

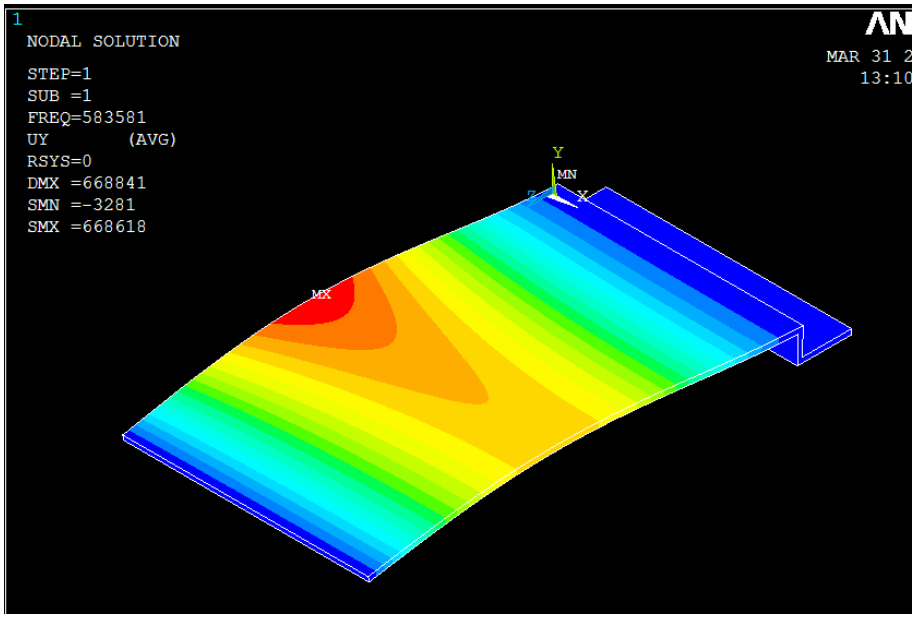

Figure 17: 2nd Mode Shape of ¼ Section Beam with *L/w*=2 and *L/g*=30.

A script was created to vary the *L/w* and *L/g* aspect ratios and run the ANSYS model for stiffness and natural frequency. Figure 18 shows the non-dimensional stiffness coefficient $D_k = k * 12L^3/(E*w*t^3)$, versus *L/g*.

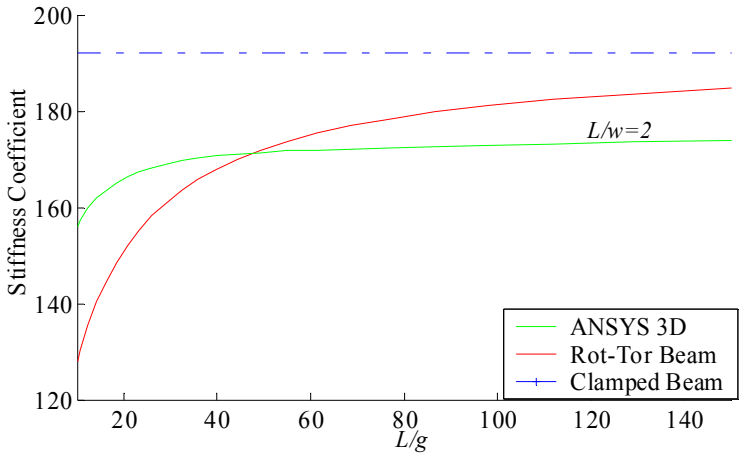

Figure 18: Non-dimensional Stiffness Coefficient versus *L/g*.

Figure 19 shows the non-dimensional stiffness coefficient, versus *L/w*. For the linear clamped beam model D_k is simply equal to 192, and it is very evident that for *L/w* < 2 or *L/g* < 40, the stiffness coefficient decreases up to 40%. The ANSYS simulation noted as *L/g*= Infinity is a 3D plate model with clamped edges.

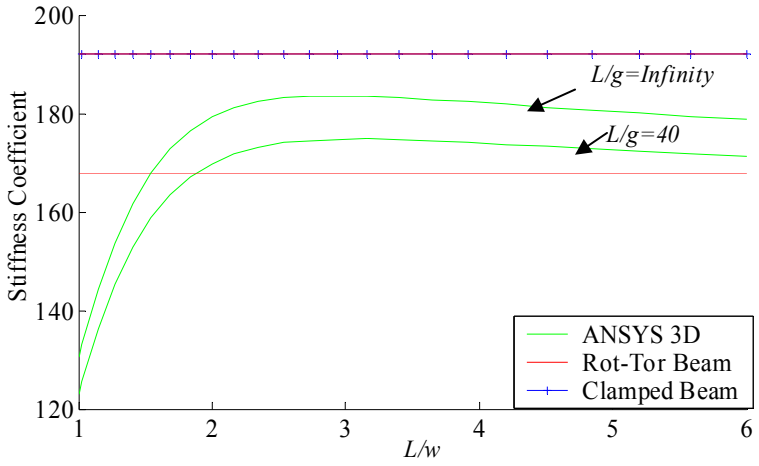

Figure 19: Non-dimensional Stiffness Coefficient versus *L/w*.

The ANSYS results are plotted along with the Clamped beam, Uniform Rotational Elastic (Boundary Condition) beam, Clamped-Clamped Plate, Uniform Rotational Elastic BC Plate theories. Figure 20 shows the eigenvalues versus L/w for $L/g = 40$.

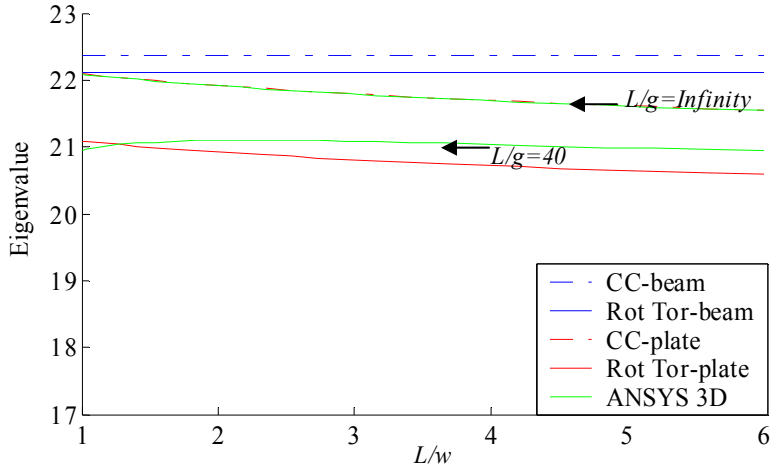

Figure 20: Eigenvalues versus L/w for $L/g = 40$ (ANSYS and Theoretical).

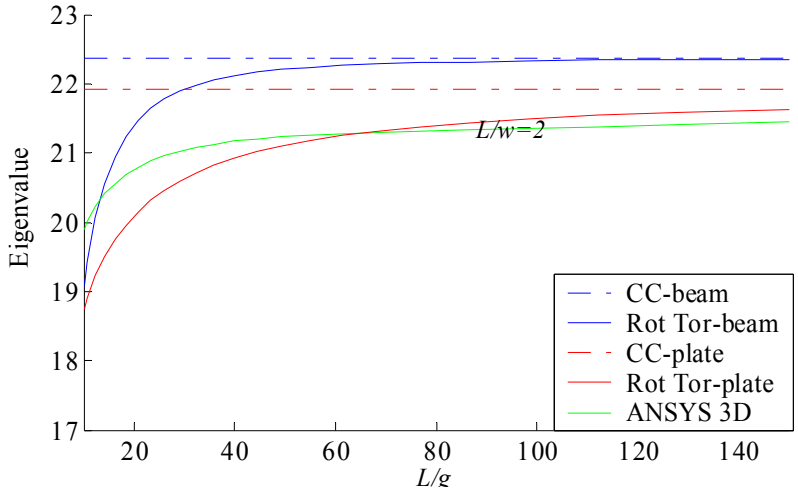

Figure 21: Eigenvalues versus L/g for $L/w = 2$ (ANSYS and Theoretical).

It is evident in Figure 20 - Figure 21 that the ANSYS simulation differs from the plate model slightly and for $L/w < 2$ or $L/g < 40$ the clamped beam model is off by up to 15%. The plate model assumes no coupling between the sidewall and top plate, and a uniform boundary condition across the plate edge, which may not apply for all geometries.

CHAPTER 4 :

EXPERIMENTAL RESULTS AND DEVICE VALIDATION

4.1 Experimental Setup

Experiments were conducted to measure device characteristics such as structure stiffness, dynamic response, optical output versus DC actuation and actuation range. Frequency response and optical output curves were obtained using the experimental setup, shown in Figure 22.

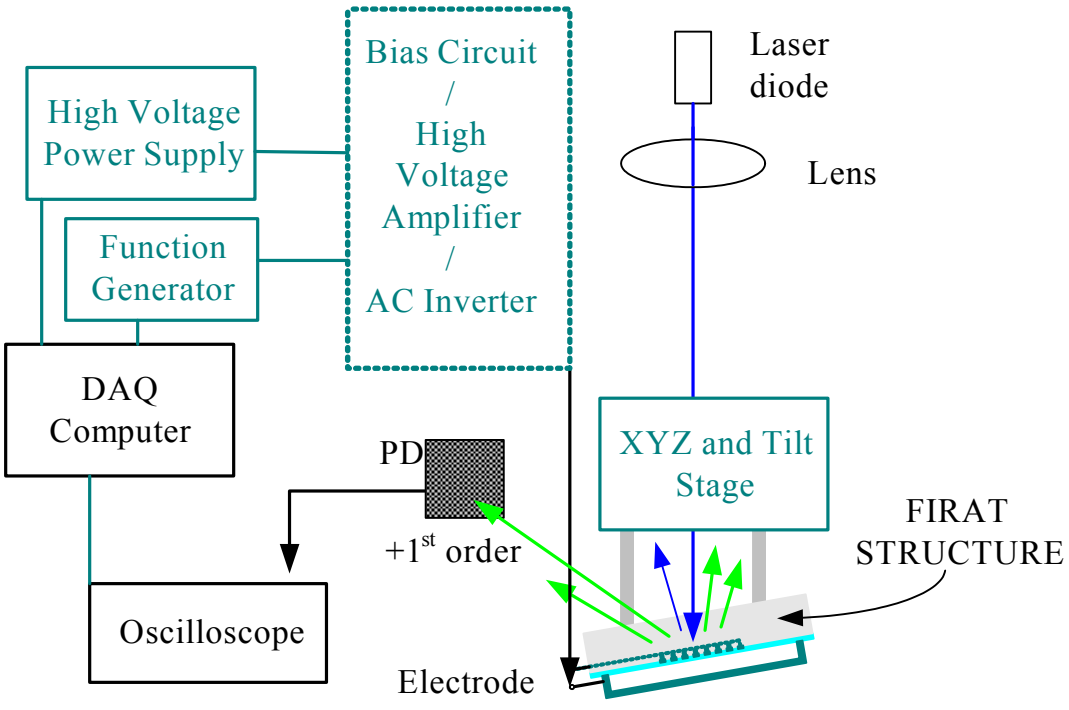

Figure 22: Experimental Setup for Testing FIRAT Structures.

The coherent light source was provided by a He-Ne Laser of wavelength 634 nm. Laser spot size was around 20 μm, via a converging lens with a 15 μm pinhole at the focal

point, a collimating lens and then a final lens focused on the grating. A photodetector with built in adjustable gain amplifier was used to measure the 1st reflected order intensity. The bias circuit was used for frequency sweeps to acquire dynamic response data. Optical output curves were obtained by using the high voltage amplifier to apply a 2 Hz triangular wave voltage input. Second flexural mode frequency response was measured using the bias circuit in combination with the voltage inverter.

4.2 Device Stiffness

Device stiffness was measured using a commercial AFM with calibrated cantilevers. Stiffness was calculated by measuring the sensitivity upon the substrate and upon the device itself. Knowing the stiffness of the cantilever, the two can be treated as springs in series, and the bridge stiffness is then found. Two different calibrated cantilevers were used in the experiment, one a 3.80 N/m stiffness, 225 μm long Veeco FESP and the other 47.2 N/m stiffness, 125 μm long Veeco TESP. Both cantilevers were calibrated themselves, via Veeco tip-less calibration cantilevers. The TESP and FESP cantilevers were calibrated by measuring sensitivity pressing upon the substrate and then pressing upon the calibration cantilever.

The stiffness of the calibration cantilever is calculated by measuring the sensitivity in mV/nm, when pressing on a solid surface and when upon a calibrated cantilever without a tip. The equation for calculation the cantilever stiffness, K_C, is given by Equation 4.1,

$$K_C = K_{ref}(C_S - C_T)/C_T * \cos(\vartheta) \qquad (4.1)$$

where K_{ref} is the stiffness of the calibration cantilever, ϑ is the angle of the tip to the calibration cantilever (about 7-8 degrees), C_S is the force curve slope on the substrate, and C_T is the combined force curve slope or sensitivity in mV/nm, when pressing on the cantilever.

The uncertainty of the reference cantilever is stated to be 1.4 N/m for the 33.87 N/m reference. The measured uncertainty of C_T was 2.9 mV/nm using a 95% CI, and 4.35 mV/nm for C_T similarly. The uncertainties were calculated by taking a sample of 5 to 10 measurements and using 2 times the standard deviation of the sample measurements as the uncertainty. The propagated error in the cantilever stiffness, U_{Kc}, is given by Equation 4.2,

$$U_{K_C} = \left(\frac{U_{K_{ref}}(C_S - C_T)}{C_T} + \frac{U_{C_S} K_{ref}}{C_T} + \frac{U_{C_T} K_{ref} C_S}{{C_T}^2} \right) \cos(\vartheta) \qquad (4.2)$$

where U_{Kref}, U_{Ct} , U_{Cs} are the relative uncertainties of each quantity named previously. For the 33.87 N/m cantilever this resulted in an uncertainty of the reference cantilever of 1.41 N/m.

The stiffness of the bridge K can be calculated using Equation 4.3,

$$K = K_C C_S / (C_T - C_S) * \cos(\vartheta) \qquad (4.3)$$

where C_S is again the force curve slope on the substrate, and C_T is the combined force curve slope when pressing on the bridge structure. The uncertainty of the cantilever stiffness can be calculated using Equation 4.4,

$$U_K = \left(\frac{U_{K_C} C_S}{(C_T - C_S)} + \frac{U_{C_T} K_C C_S}{(C_T - C_S)^2} + \frac{U_{C_S} K_C}{(C_T - C_S)} + \frac{U_{C_S} C_S K_C}{(C_T - C_S)^2} \right) \cos(\vartheta) \qquad (4.4)$$

As C_T approaches C_S the uncertainty becomes large, this is the case when the bridge device being tested is approximately more than 3 times the stiffness of the calibrated cantilever. For these cases the uncertainty will become large and not negligible. The stiffest calibrated cantilever that was used was 47 N/m, therefore stiffness measurements made on bridges approaching 140 N/m were not as accurate. Table 3 shows some example experimental measured parameters and the propagated uncertainty, along with the experimentally calculated stiffness and theoretical value accounting for large gaps but not large *L/w* aspect ratios.

Table 3: Example Experimentally Measured Stiffness and Uncertainty.

L	w	C_T	U_{C_T}	C_S	U_{C_S}	K	U_K	K_{th} *w/Rot*
150	50	320	5.0	82.2	1.9	16	1.3	17
100	50	185	2.0	82.2	1.9	38	3.4	61
60	50	110	2.0	82.2	1.9	140	27	262
80	50	145	2.0	82.2	1.9	62	7.0	116
60	40	117	2.0	82.2	1.9	110	18	168
60	20	137	2.0	82.2	1.89	71	8.7	84
120	100	184	5.6	82.5	0.78	39	3.9	55

As the stiffness increases from 40 to 140 the uncertainty of the measurement increases almost 10 times the previous value. Also the 2D model of the beam is no longer valid soon after the beam aspect ratio decreases below around 2. The dependence upon aspect ratio was analyzed before using the FEM model in the theoretical section.

Several different batches of devices were probed with the calibrated cantilever to measure the stiffness of each. Each batch has relatively similar gap height and film thickness, barring any un-uniformities. By testing a variety of devices the dependence of

stiffness upon beam geometry was quantified. Figure 3 shows the experimentally measured stiffness in red, along with contours that display the theoretical models approximation.

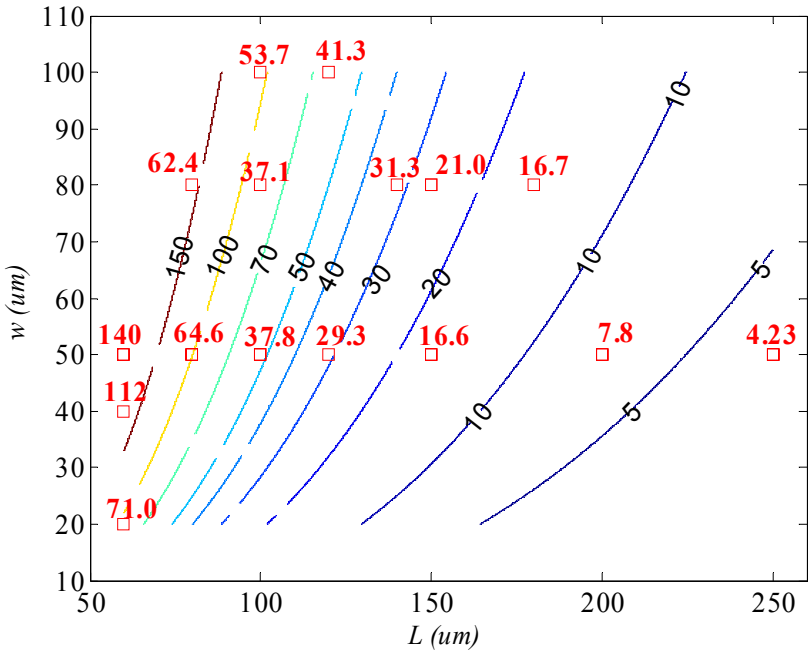

Figure 23: Contour Plot of Theoretical Stiffness with Experimentally Measured Data.

Note that the experimentally measured values, for large aspect devices, are slightly lower than expected from the theoretical 2 D model.

In order to show the dependence of the stiffness on the length and gap aspect ratios, a non-dimensional stiffness coefficient was calculated and plotted along with the theoretical and ANSYS 3D models. A large number of the devices fabricated have aspect ratios less than 2, and under point loading at the center of these bridges, the deflection is not uniform throughout the beam's width cross section. Figure 24, on the following page, shows the non-dimensional stiffness coefficient $D_k = k * 12L^3 / (E*w*t^3)$, for the clamped beam, rotational torsion beam and ANSYS 3D model, graphed vs. L/w.

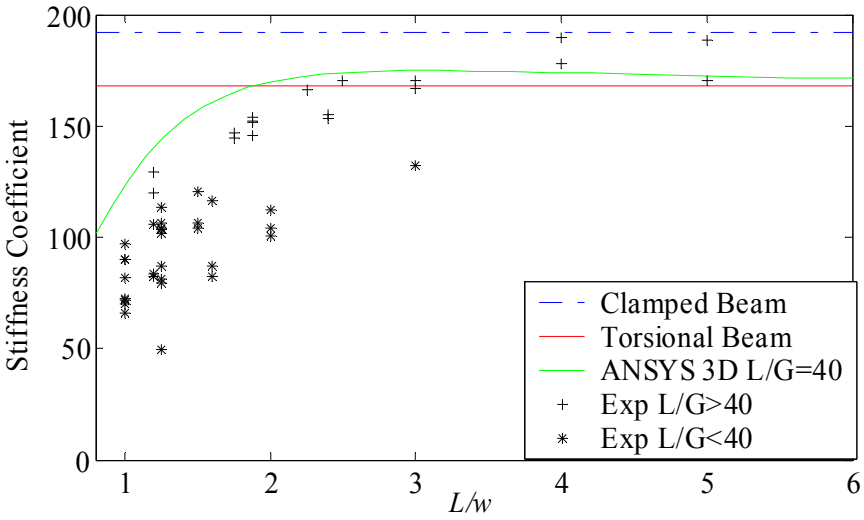

Figure 24: Comparison of Stiffness Coefficient versus *L/w*.

The ANSYS model was run for an *L/g* ratio of 40 and experimental data is shown for *L/g* less than 40 and *L/g* greater than 40. The experimental data verifies the general trend of the ANSYS model and validates the necessity for a 3D model of devices with aspect ratios less than approximately 2. Figure 25 shows the non-dimensional stiffness coefficient for the clamped beam, large gap beam (using uniform rotation elastic boundary conditions) and ANSYS 3D model, graphed versus *L/g*.

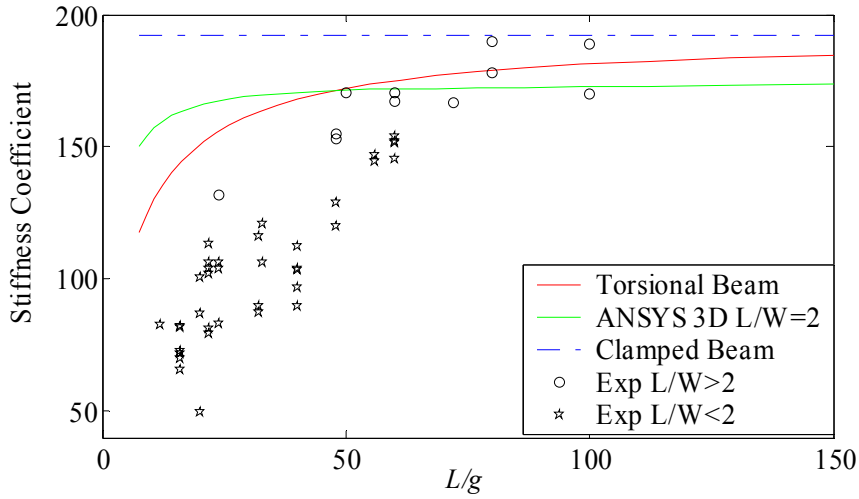

Figure 25: Stiffness Coefficient versus *L/g*.

The ANSYS model was run for an *L/w* ratio of 2 and experimental data is shown for *L/w* less and greater than 2. The experimental data, again verifies the general trend of the ANSYS model and validates the necessity for a 3D model of devices with gap aspect ratios less than approximately 50.

Although the trend is clearly evident in the above figures, there is a substantial amount of scatter to the data. Several factors could easily be contributing to this. As discussed previously, the very stiff devices had a large amount of uncertainty present due to the choice of calibration cantilever. Also, the calculation of the non-dimensional stiffness coefficient is very dependent on the thickness measurement, as it scales with the inverse cube. If the measured thickness is slightly off the calculation will suffer. The value used for elastic modulus was for bulk aluminum [16]. Since the aluminum bridge material is a sputtered thin film, its mechanical attributes may not be exactly that of bulk aluminum. Also, further characterization of the material properties such as the film's intrinsic stress may also prove for a more complete analysis.

4.3 FIRAT Dynamic Response

The dynamic response of the bridge structures was investigated by performing a frequency sweep of a constant amplitude AC signal that is biased externally in order to perform the experiment at the maximum sensitivity point of the optical curve. The AC driving voltage was small compared with the DC bias to prevent frequency doubling and also to keep the photo detector within the linear range. The frequency output was recorded and plotted in decibels on a logarithmic scale. The transfer function governing dynamic response, as given in Section 2.2.3 was then used as a basis to curve fit the experimental data with the analytical model. This same curve fit was performed on a

variety of devices in order to understand their response and see if the model was appropriate. A summary of frequency response data is listed in Table 4.

Table 4: Summary of Frequency Response Data Comparing Theoretical and Experimental Fit Parameters.

Length (um)	Width (um)	Thickness (um)	gap (um)	Natural Frequency Theoretical (kHz)	Natural Frequency Experimental (kHz)	Q Theoretical	Q Experimental
60	20	0.96	2.30	1267	1094	14.03	12.82
60	50	1.03	2.52	1372	1201	5.43	6.17
60	50	0.95	2.51	1266	1008	4.34	5.66
80	50	0.75	4.60	546	270	5.98	2.16
80	50	0.95	2.68	720	652	2.09	3.01
80	80	0.77	4.80	558	403	2.79	4.26
80	80	0.77	4.60	560	431	2.47	4.92
80	80	0.88	2.20	672	444	3.12	1.80
100	50	0.86	5.50	402	338	8.64	5.34
100	50	0.86	5.50	402	291	8.64	8.40
100	50	0.77	4.60	365	233	4.10	3.52
100	50	0.75	4.60	355	226	3.87	5.09
100	50	1.03	2.64	504	454	1.41	1.37
100	80	0.78	4.60	372	269	1.62	2.97
100	80	0.68	4.60	321	292	1.19	3.59
120	50	0.98	2.85	332	270	1.07	1.46
140	80	0.84	4.40	208	142	0.83	2.00
140	80	1.04	2.90	261	233	0.92	0.92
150	50	1.00	2.69	219	257	0.58	0.83
150	80	0.95	5.70	202	116	2.06	1.98
150	80	0.95	5.70	202	93	2.06	1.57
150	80	0.94	5.30	201	114	1.62	2.42
150	80	0.96	2.40	212	169	1.48	1.05
180	80	1.04	2.80	159	157	0.94	0.82
250	80	0.97	7.00	75	70	1.46	1.76
250	80	0.97	7.00	75	57	1.46	2.03
250	80	0.95	7.00	74	54	1.40	2.14
250	80	0.97	7.00	75	74	1.46	3.03
250	80	1.02	2.01	82	92	2.12	2.51
250	100	1.02	2.15	82	110	2.80	2.04
300	100	0.99	3.20	55	23	1.05	1.03

In general, the theoretical model predicts the dynamic characteristics of the fabricated devices given in Table 4. The model is subject to propagated error from measurement of devices dimensions, and also other factors that were not accounted for such a film stress, true structure shape and uniformity of the aluminum thin film that the

bridge layer is composed of. Even so, the important information, such as changes in damping and bandwidth with varying dimensions, is predicated well enough for use as an efficient model in device design and optimization.

By understanding the dynamic response the structure dimensions can be tailored to the preferred imaging application. In example, Figure 26 gives the frequency response curves of two 150 x 80 µm bridge structures, of which have similar bridge thickness but different gap heights. One is 2.4 µm and the other is 5.7 µm, and each device has a similar stiffness around 12 N/m, suitable for tapping mode experiments. The device with gap of 5.7 µm has a Q of around 2, while the smaller gap device is over damped.

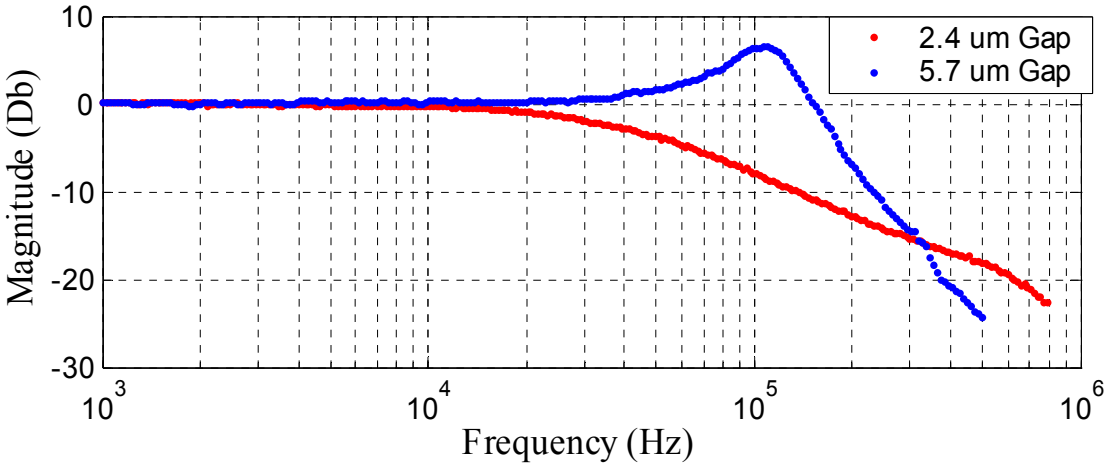

Figure 26: Frequency Response of 150 x 80 µm Bridge Structures with Gap of 2.4 µm and 5.7 µm.

This device demonstrates the advantage of adjusting the gap height for a desired application, both the 2.4 and 5.7 µm gap devices will have a similar stiffness, yet the larger gap device has bandwidth at least six times that of the 2.4 µm device, making it more suitable for tapping mode experiments. Figure 27 shows the experimental and theoretical frequency response for a 60 x 20 µm bridge structure.

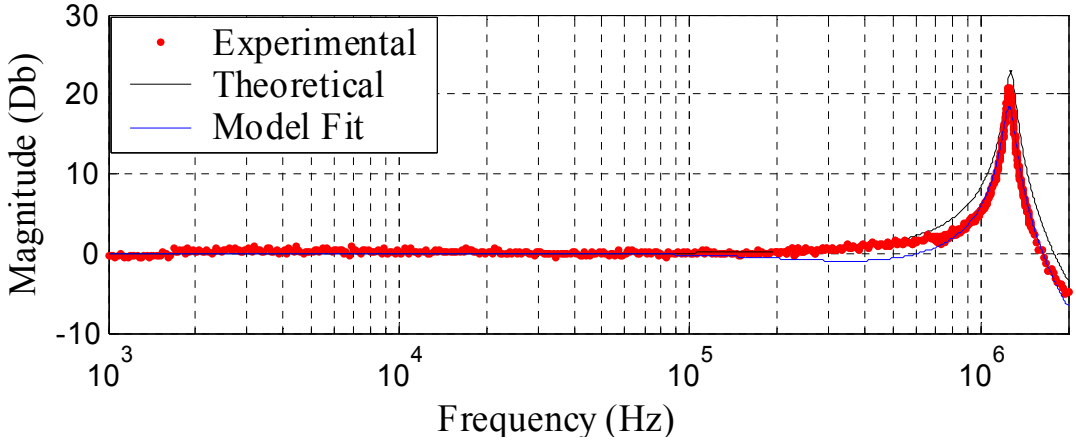

Figure 27: Frequency Response of 60 x 20 µm Bridge Structure with Gap of 2.3 µm and Thickness 0.96 µm.

The theoretical model and experimental curve fit, for this device, both match the data well. The theoretical Q for this device was 14.03 and the experimental fit value is 12.82. This structure's high Q and bandwidth (greater than 800 kHz), makes it suitable for fast imaging applications. The optical modulation of this device was near 85%, its collapse voltage was 145 Volts DC, and the measured stiffness was 64 N/m, therefore this structure would be suitable for fast imaging applications.

The goals of the design and characterization were to provide a baseline model for fabricating imaging devices and show improved dynamics over the previous generation of FIRAT devices. The ability to fabricate bridge devices with gap thickness of at least 6 µm has been demonstrated. Similar 60 x 20 µm bridges have been successfully fabricated with gap thickness of 5.5 µm and aluminum bridge thickness of 0.6 µm. Based on the model and experimental data, such devices should have Q of around 100 and stiffness of 15 N/m, making them suitable for fast imaging.

4.4 Dynamic Response with 2nd Mode Actuation

Actuation of the 2nd mode was performed by driving the two symmetric electrodes with AC signals that were 180 degrees separated in phase, while having the same amplitude and bias. In this experiment, it was validated that the 2nd mode of FIRAT structures, with dual electrodes and dual optical readout, could be actuated using the 2nd mode shape. It is also important to show that the 2nd mode was less damped that the 1st. This provides the motivation for placing a tip offset to one side for use in tapping mode experiments, as it would allow for higher bandwidth and less damping. In friction experiments, the tip would be mounted at the center 2nd mode node point. Figure 28 shows w micrograph of an example 200 x 80 μm dual electrode structure with a 4.5 μm gap.

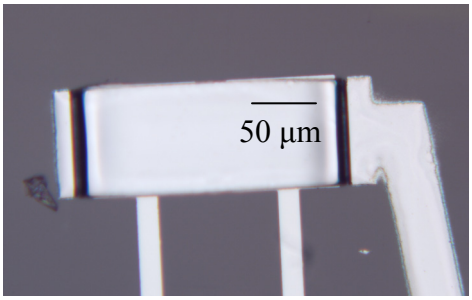

Figure 28: Micrograph of 200 x 80 μm Dual Electrode Bridge Structure.

The experiment was conducted using only a single laser spot that could be moved from one grating to the other but did not allow measurement simultaneously. The gratings are orientated at 30 degrees rotation from one another allowing measurement of reflected orders simultaneously from either grating, if dual beams or an elliptical laser spot is used. The frequency response data was collected similarly to that of the single electrode devices. Figure 29 shows the frequency response of a 140 x 80 μm dual

electrode bridge structure with actuation of both 1st and 2nd flexural modes separately, along with the theoretical response and experiment fit curves.

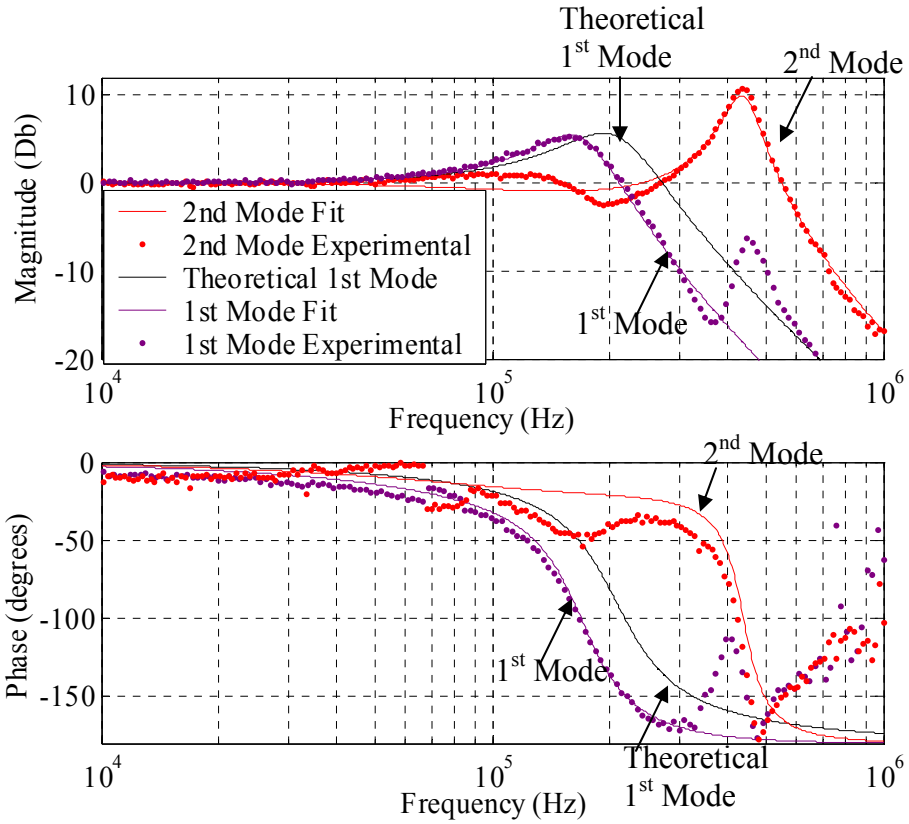

Figure 29: Frequency Response Data from Dual Electrode, 140 x 80 µm Bridge Structure with 4.4 µm Gap.

The dynamic response model was fit to both the 1st and 2nd flexural modes, and fit parameters were found. Under 2nd flexural mode actuation the *Q* and bandwidth is more than double that of the first mode. Table 5 shows the experimental and theoretical frequency response parameters for the 1st and 2nd flexural modes. The 2nd flexural mode Q is nearly double that of the first mode. The theoretical lumped squeeze film damping model is based on a flat plate moving back and forth squeezing the air out of the gap (basically the 1st mode motion). Since the 2nd flexural mode is fully axisymmetric, the damping mechanism is different than the 1st, slip-film viscous damping rather than

squeeze film damping. The 2nd flexural mode Q is much higher because of this difference in damping mechanism.

Table 5: Experimental and Theoretical Parameters for 1st and 2nd Flexural Modes of Dual Electrode Device.

	Experimental Natural Frequency (kHz)	Theoretical Natural Frequency (kHz)	Q Experimental	Q Theoretical
1st Mode	139	205	2.16	1.85
2nd Mode	338	584	4.89	-

Under electrostatic actuation, superposition modes will become more present with increasing damping [21]. Although the dual electrode device that was tested is not over damped, it is evident in Figure 29 that there is coupling between modes. With decreasing gap and increasing width/length, this becomes even more prevalent, as was seen in frequency response data from longer length/width or 2.4 μm gap, dual electrode devices. A theoretical value for the 2nd flexural mode is not shown as the squeeze film damping model in not valid for that mode shape. Differences between theoretical and experimental data may be due to the approximate modulus or compressive stress in the structure, which can shift the resonance frequency.

With the 140 x 80 μm device 2 times the Q and bandwidth has been demonstrated, similar devices of higher Q could be fabricated with widths of 40 or 50 μm, while still possessing reasonable modulation and actuation voltage. The collapse voltage on the device tested here was around 75 V and optical modulation of 85%. Dual electrode devices, like these could be useful for friction experiments or for tapping mode utilizing an offset tip.

CHAPTER 5 :

FIRAT WITH EXTENDED OPERATION RANGE

5.1 Increased Actuation Range FIRAT Structure

In order to utilize the increased range interferometer, the actuation range of the structures must be increased. Since the collapse height is approximately $^2/_3$ of the original gap, the actuation distance can be increased effectively by raising the gap thickness. Previous generation FIRAT devices were limited to approximately 0.7 µm of actuation range. With a gap height of 5.7 µm, actuation distance greater than 2 µm is demonstrated. The bridge device tested collapsed at 102 Volts, after it had displaced nearly 2.1 µm. The actuation distance was measured using an optical prolifometer. Figure 30 shows the DC actuation curve for the 150 x 80 µm bridge device.

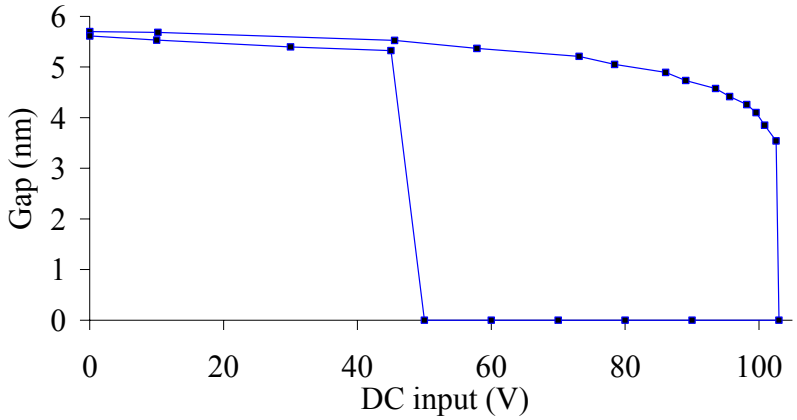

Figure 30: DC Actuation Curve for 150x80 µm Device with 5.7 µm Gap.

By also measuring the optical curve output versus input voltage, the optical output can then be correlated to the actuation distance. Figure 31-A displays the optical output from the 1st order versus the input voltage.

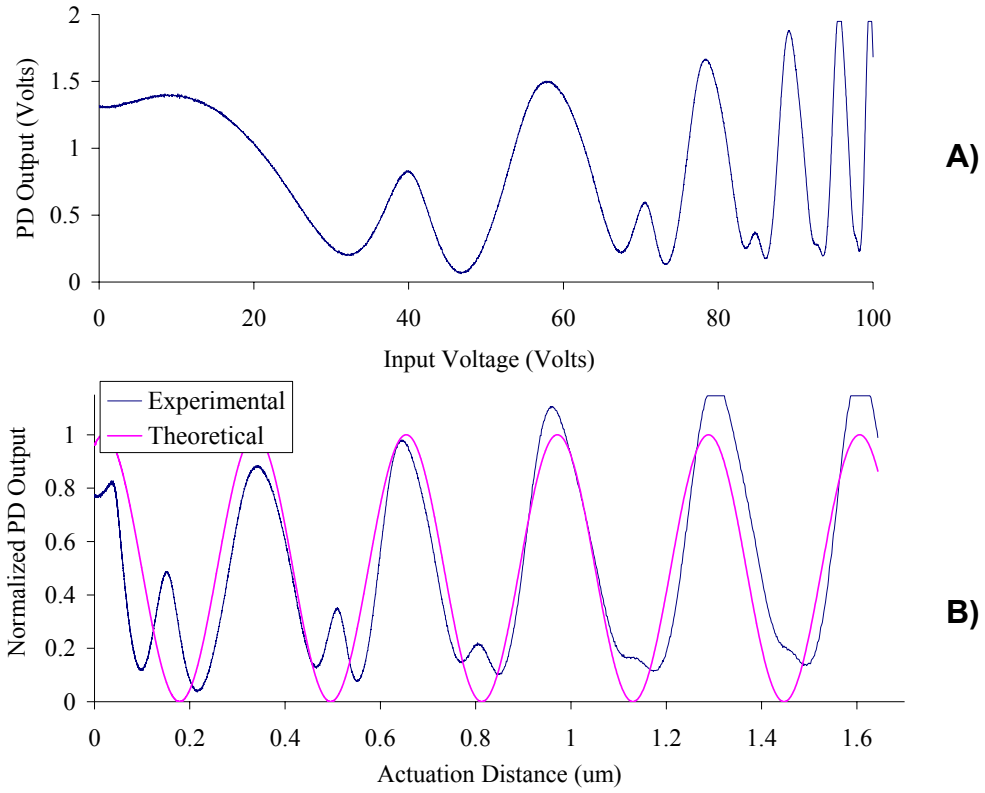

Figure 31: A) Optical Output Curve under Electrostatic Actuation. **B)** Normalized Optical Output Curve versus Actuation Distance.

The optical modulation can be estimated by taking peak-peak voltage difference divided peak voltage. The modulation of the above device is 92%. By correlating input voltage to distance, the experimental and theoretical optical curves were plotted versus actuation distance in Figure 31-B. The experimental optical curve follows the sinusoidal trend of the theoretical output well. The saddles that appear at the bottom of each cycle may be due to polarization of the laser or reflections in the quartz substrate. They are present on many of the devices fabricated, but not all of them. Also, the optical output cycles noticeably change as the voltage is increased. This could be due to the fact that the bridge surface deforms during application of the electrostatic load, changing the shape of the surface which the laser spot is reflected.

5.2 Extended Detection Range via Side Sensing Device

Several bridge structures were fabricated that could be used for contact mode imaging. These structures ranged in stiffness from 1 N/m to 15 N/m. In order to increase the imaging range, a long bridge structure is used and the laser spot is focused far to one side of the grating, which runs the full length of the structure. Although this will result in some loss of sensitivity it is a simple way of increasing the imaging range, without using phase –shifted grating. The device can also be used normally with the spot at the center of the beam. A proof of concept experiment was completed using a 300 x 100 µm bridge structure with 3.15 µm gap size.

In order to show the feasibility of obtaining increased range, the device was actuated using a fully offset triangular wave signal at a very low frequency (2 Hz). Optical output signals are shown versus the input voltage with the Laser at center and at the left side of the bridge, in Figure 32.

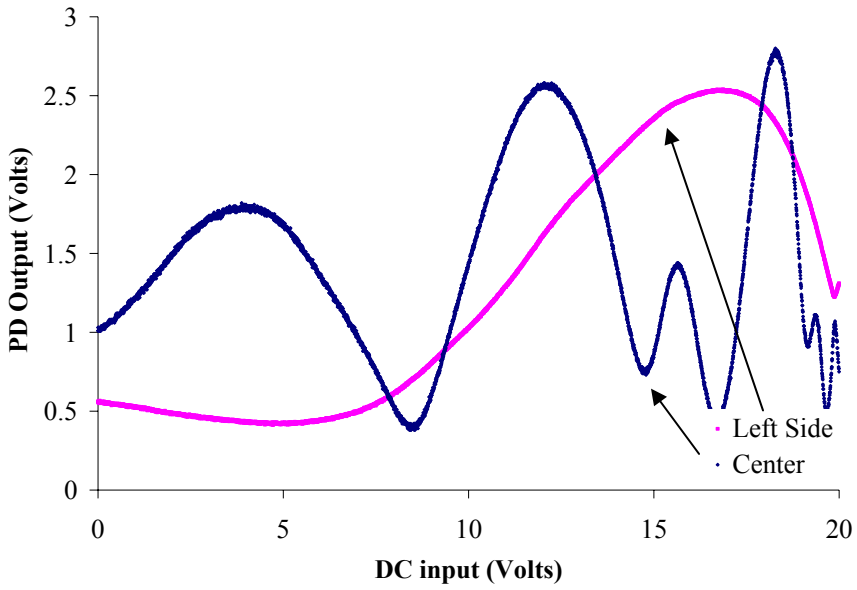

Figure 32: Optical Output Curves from the First Order, with Laser Spot in Center of Bridge and at Left Side.

The maximum voltage applied at the peak of the triangular was 20 volts. First the spot was focused at the center of the bridge and the resulting intensity signal from the photo receptor was recorded. Next the laser spot was moved to the left edge of the bridge and the optical curve here was also recorded.

From visual inspection of both curves it is evident that the center optical curve goes through roughly 1 ½ cycles while the left side goes through only a ½ cycle. Since each ½ cycle of the optical curve is λ/4 (158.5 nm for λ = 634 nm), the range of the left side implementation is 3 times that of the center configuration (475.5 nm for λ = 634 nm). The estimated sensitivity at the center is 38.8 mV/nm and at the left side 13.2 mV/nm, therefore 3 times the increase in range costs the same proportion in sensitivity.

5.3 Dual Phase Shifted Interferometer

5.3.1 Overview

The phase shifted sensor structure is fabricated using an aluminum bridge above a pair of symmetrically placed optical diffraction gratings with period of 4 μm. The device is fabricated upon a polished quartz wafer and the bridge/gratings serve as an integrated electrode for electrostatic actuation. To obtain displacement data a He-Ne laser is focused on the grating and the intensities of resulting reflected orders are measured using a photodetector. On one side of the grating, the quartz between the grating fingers was etched a specified depth depending on the wavelength of the laser being used. This creates a difference in path length between the light waves going through the left and right hand gratings. By creating an optical path length difference of about λ/8, a 90

degree phase shift between the optical intensities output curves of the two gratings is induced. Figure 33 the schematic of the device structure.

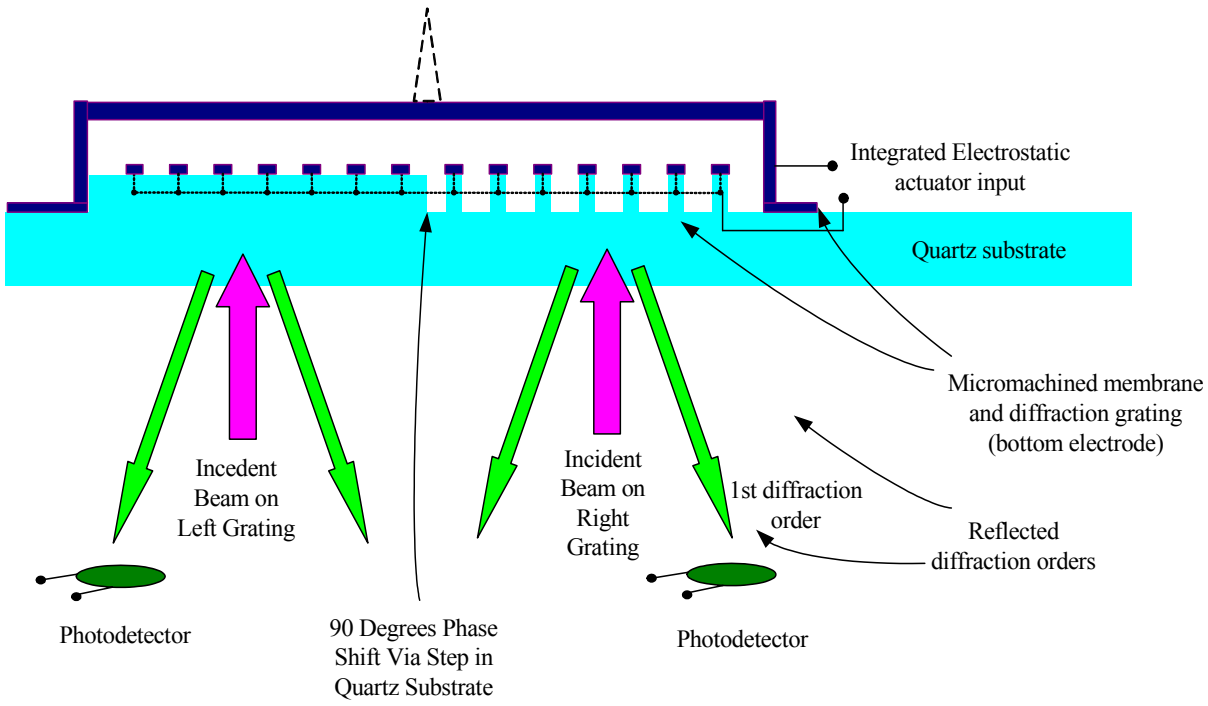

Figure 33: Schematic of Structure with Increased Range Interferometer.

When utilizing this structure for tapping mode microscopy, the combination of both grating outputs will allow for measurable range greater than the previous limitation of λ/4. With the addition of a sharp tip, this phase sensitive interferometer, with integrated actuator and dual phase-shifted optical readout, should provide increased detectable range for force spectroscopy and other imaging applications when utilizing the FIRAT type sensor [10].

5.3.2 Phase Sensitive Diffraction Grating and 90 Degree Shift Theory

The combination of an optical reflector, the aluminum bridge structure, spaced above a reflective grating, with period d_g, is a phase sensitive diffraction grating [13, 14]. For structures with equal pitch reflective grating and transparent slit, the intensities of the resulting orders are given by Equation 5.1 [15],

$$I_0 = I_{in}\cos^2\left(\frac{2\pi(d+\phi)}{\lambda}\right)$$
$$I_{\pm 1} = \frac{4I_{in}}{\pi^2}\sin^2\left(\frac{2\pi(d+\phi)}{\lambda}\right) \qquad (5.1)$$

where I_{in} is incident laser intensity, and d is distance between the reflector and grating, and ϕ is the optical path length shift. If on grating has zero shift, in order to have a 90 degree phase difference between intensities outputs of two gratings ϕ must be equal to λ/8. By equating this phase shift to the physical layout of our device Equation 5.2 is derived, which gives the required etch depth, d_e, of the quartz substrate on the shifted grating.

$$d_e = \frac{\lambda}{8(\eta_{ox} - 1 + \alpha_{step})} \qquad (5.2)$$

where η_{ox} is the index of refraction of the substrate (1.5 for quartz) and α_{step} is the proportion of the etch depth, that the aluminum bridge will shift downward, on the etched side of the device, because of the conformal sacrificial layer. Using our fabrication process a resulting etch depth of around λ/8 is required. Figure 34-A shows the normalized intensity of the first order versus normalized gap distance for both grating outputs.

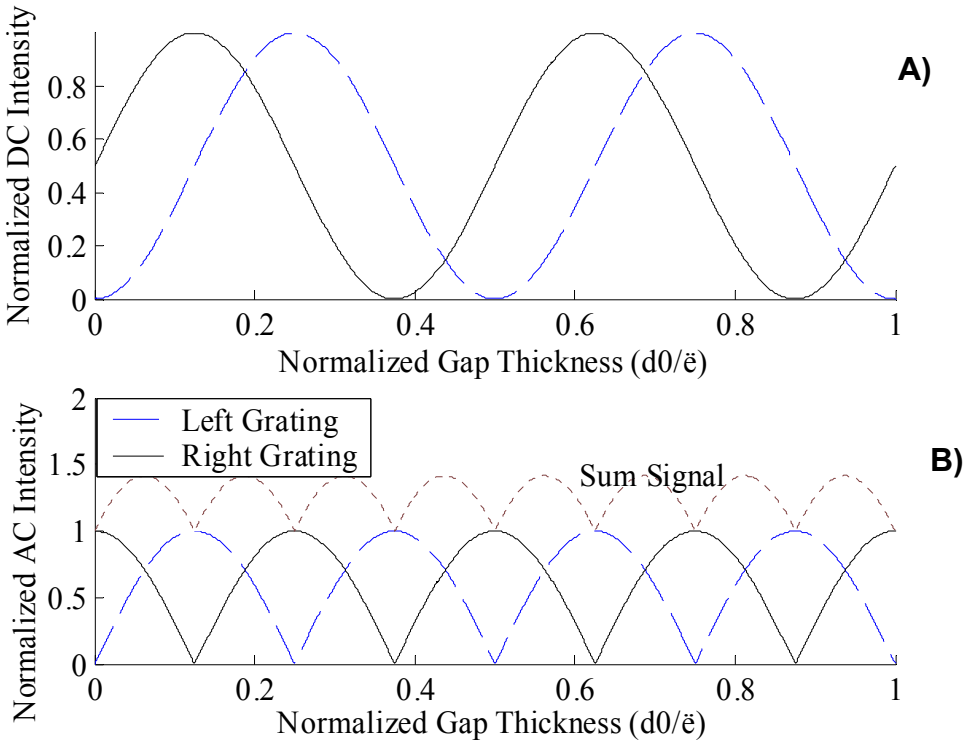

Figure 34: **A)** Theoretical normalized intensity versus normalized. **B)** Theoretical amplitude of the AC component of PD intensity

Note that the two optical output curves are 90 degrees out of phase. The AC signal that results from the photodetector, when a small oscillatory motion (much smaller than λ/8) to the reflector, is important for tapping imaging. The resulting normalized AC amplitude of the intensity output could be approximated, for small oscillations, by Equation 5.3.

$$I_{AC\ Norm} \propto \frac{\partial \mathrm{I}_1}{\partial d} \propto \left|\cos\left(\frac{2\pi(d+\phi)}{\lambda}\right)\sin\left(\frac{2\pi(d+\phi)}{\lambda}\right)\right| \qquad (5.3)$$

Figure 34-B shows the theoretical normalized AC amplitude of the intensity, for small oscillations (much less than λ/4), about an increasing normalized mean gap thickness. The theoretical optical signals are shown for two gratings that are shifted by λ/8 and the resulting sum of both.

5.3.3 Fabrication Process

The device structure and fabrication process used to facilitate the 90 degree phase shift is similar to the previously described fabrication process. The modified process flow is shown in Figure 35.

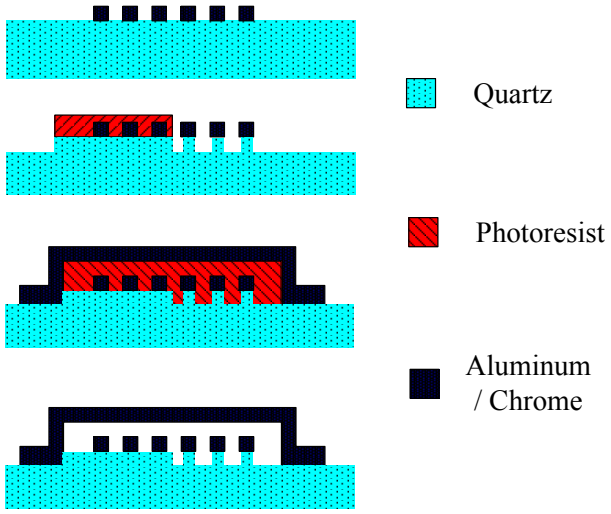

Figure 35: Modified Process Flow for Phase Shift Device.

First step in phase shift device process flow is patterning of a 4μm period diffraction grating upon a quartz substrate. The grating is patterned the same as other devices, accept a 10 nm layer of chrome is used as the top layer of the grating, to prevent etching of the aluminum and to serve as a hard mask during the standard oxide process, reactive ion etch. The quartz that lies between the fingers on one side of the device, is etched around 80 nm using a reactive ion etch. This provides the desired optical path length shift between gratings spaced symmetrically on either side of bridge. The etch depth was characterized using a contact prolifometer. Because the RIE was not completely uniform throughout the wafer, the etch depth varied 83 nm +- 10 nm, but was uniform in the locality of specific devices or throughout each chip.

Next the resist is patterned for the sacrificial layer. Figure 36 shows a prolifometer scan of the sacrificial layer on a phase shift device.

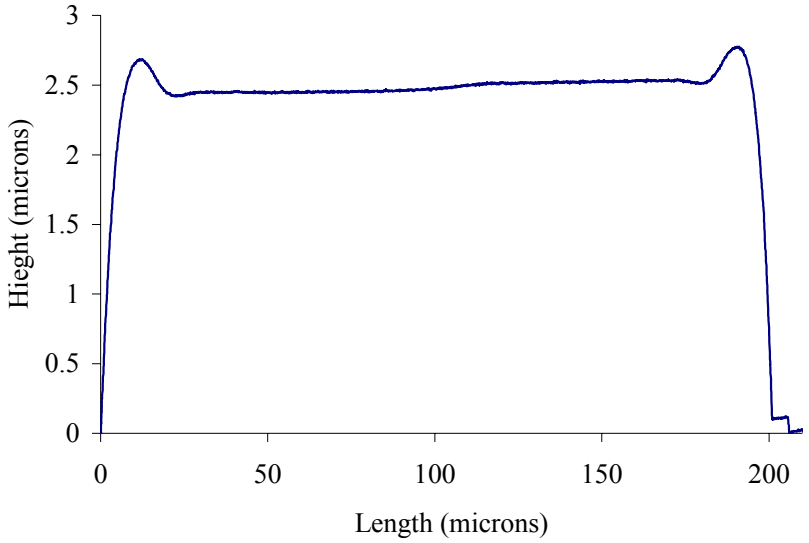

Figure 36: Prolifometer Scan of Sacrificial Layer on Phase Shift Device.

Which, after hardbake, showed a slight step due to the etching of the quartz substrate, between the gratings on one side of the device. The magnitude of this step was usually around one half of the etch depth, depending on the soft and hardbake used in patterning the resist. The structure is completed with the aluminum bridge deposition/patterning. Figure 37 is a SEM image of a released device.

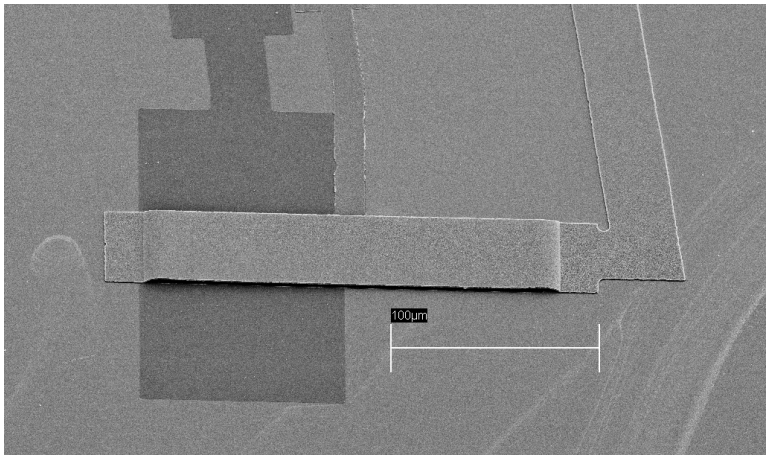

Figure 37: SEM Image of Device with Phase Shift Interferometer.

The device dimensions are approximately 50 μm wide, 200 μm long, 0.9 μm thick (bridge thickness), and 2.5 μm gap thickness. The etch dept in the quartz wafer is 83 nm, measured with a contact prolifometer, and the step in the membrane is approximately half of that value, measured with an optical prolifometer.

5.3.4 Experimental Validation

A proof of concept experiment was conducted using the device shown in Figure 37. A He-Ne Laser (λ =634nm) was used to illuminate the grating through the backside of the quartz substrate, focusing on either grating at an angle of 5º. The spot size of the Laser was roughly measured at about 20 μm. To facilitate movement of the Laser spot from one grating to the other, the structure was mounted on a 3D stage. A change in the reflected orders was visually observable as the Laser spot was moved from one side to the other.

The bridge was actuated with a 1 kHz AC signal that decreased proportionally to the DC bias, in order to keep the oscillatory motion relatively constant (target about 10nm). The DC bias was swept from 5 to 23 Volts, while measuring DC and AC coupled photodetector signal, from the 1st diffraction order, at each step. The previous experiment was repeated for both gratings. Figure 38-A, on the following page, shows the experimentally measured optical curve versus applied DC bias for each grating. The bridge structure is electrostatically actuated with a 1 kHz AC signal that is adjusted inversely proportional to the DC bias in order to keep the membrane oscillation at around 10 nm. Both signals from the right and left gratings are shown along with the sum of the two.

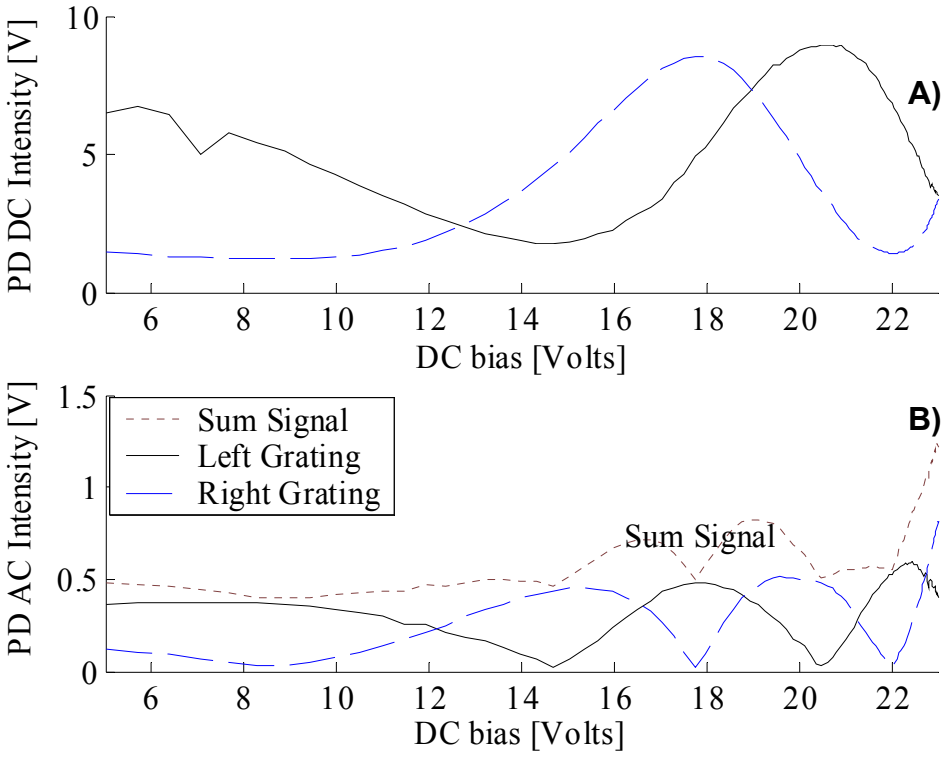

Figure 38: **A)** Measured Optical Intensity versus DC Bias. **B)** Peak to Peak Amplitude of the AC Optical Intensity.

The experimental trend resembles the theoretical model (see Figure 34-A) with 90 degrees phase shift between curves. Note that the x-axis in Figure 38-A is DC bias, not displacement distance. The displacement can be measured versus DC bias using an optical prolifometer or an AFM, allowing the optical curves to be plotted versus distance. Figure 38-B shows the experimentally measured AC photodetector amplitude, from each grating, versus the applied DC bias with an applied AC amplitude starting at 1 volts peak to peak and decreasing proportionally to the DC bias. The AC input is applied in this manner in order to try to maintain a constant vibration amplitude of the device as the DC bias is increased. The shifted, and un-shifted grating curves, are again roughly 90 degrees apart. As the AC output from one grating goes to zero, the other is at its peak, therefore, by summing the two signals, the AC output signal does not decrease to zero

with each ½ optical curve cycle, as it would with only a single grating. When implemented for tapping mode AFM, this can allow measurement of displacements greater than $\lambda/4$ and are only limited by the actuation distance.

The phase shifted dual grating interferometer showed a feasible way to provide an AC tapping detection signal for a displacement detection range of 0.5 microns. The combination of the increased range displacement detection scheme and large gap devices, with 2 μm actuation range, will allow FIRAT devices to be more useful for probe microscopy.

CHAPTER 6 :

CONCLUSIONS AND FUTURE WORK

A displacement sensor was fabricated that used phase shifted, dual diffraction gratings, in order to increase the detectable range of motion using a FIRAT structure. A desired phase shift, between optical output curves can be introduced via a micromachined step in the quartz substrate below one of the gratings. The importance of the detection scheme to tapping mode probe microscopy was demonstrated by showing that both gratings can be used together in order to increase the range of displacement detection beyond that of previous implementations of this sensor type.

With the changes in design and modified geometry/fabrication process, force sensing structures with improved displacement detection range and dynamic response are demonstrated. Several devices were fabricated that exhibited a Q of 15 and stiffness 60 N/m, and could therefore be implemented for Fast Imaging Experiments. Tapping mode devices were fabricated with stiffness ranging from 1- 30 N/m and bandwidth well into 100 kHz depending on the device. A reliable process was created for fabricating devices with 5.7 μm gap thickness, these devices displayed electrostatic actuation range up to 2.2 μm with good optical modulation. Devices with stiffness ranging from 1 N/m to 140 N/m were successfully fabricated. It was demonstrated that the 2nd flexural mode shape of the bridge structure can be excited and also that it is subject to less damping than the 1st mode.

The characterization of bridge structures validated the theoretical models and displayed model limitations, such as, for devices with low gap / width aspect ratios, 2D modeling is not sufficient. The dynamic modeling provided a general idea of the response the device will exhibit, although the natural frequency and Q may have differed largely from the theoretical values, the trends were useful in predicating what device dimensions will be required for given characteristics.

The FIRAT bridge structures have been utilized for tapping mode imaging and with modifications to process parameters, such as gap and thickness, devices tailored toward their respective imaging applications can be fabricated. The previously introduced an FIRAT structures could feasibly obtain pico-newton force resolution along with increased bandwidth. With the new device structure, the range does not have to be limited to $\lambda/4$ (167.5 nm for $\lambda = 670$ nm), and the dynamic response can be chosen to suit the particular imaging application.

Similar devices used for wet AFM imaging have been fabricated using silicon nitride or other materials. These fabrication processes can be used for structures with built in oxide sharpened silicon tips, allowing for batch fabrication of "ready to use" FIRAT structures. In summary, the ability to fabricate FIRAT structures with improved dynamics was demonstrated by successfully fabricating structures with 900 MHz bandwidth and Q of 15. In addition actuation range was increased to 2.1 μm and displacement detection to 0.5 microns.

APPENDIX A:

ANSYS STATIC AND MODAL CODE

```
finish
/clear

/CWD,C:\byron\ANSYS\t8g3varyLdw
/psearch,C:\byron\ANSYS\Macros
/nerr,0,,,,0

/prep7

!Dimensions----------
t=.8e-6
Ldg=40

n=25
!------------
w_min=50e-6
w_max=100e-6

n_w=n  !# Ldws
*DIM,w,ARRAY,n_w                    ! init Length array
w_inc=(w_max-w_min)/(n_w-1)
*VFILL,w(1),RAMP,w_max,-w_inc       ! fill gap from g_min to g_max

!------------
L_max=300e-6
L_min=80e-6

n_L=n  !# Ldws
*DIM,L,ARRAY,n_L                    ! init Length array
L_inc=(L_max-L_min)/(n_L-1)
*VFILL,L(1),RAMP,L_min,L_inc       ! fill L from L_min to L_max

!----------
*DIM,Ldw,ARRAY,n
*DIM,g,ARRAY,n
*do,ig,1,n
g(ig)=L(ig)/Ldg
Ldw(ig)=L(ig)/w(ig)
*enddo

*cfopen,dim,txt
write,t
```

```
write,Ldg
writer1,'g',1
writer1,'w',1
writer1,'L',1
writer1,'Ldw',1
*cfclos

*do,iLdw,1,n
parsav,all

c_c_qtr_pl_br,w(iLdw),L(iLdw),t,g(iLdw)

*cfopen,k_s,txt,,append
write,k_stiff
*cfclos

*cfopen,f_n,txt,,append
writer1,'fn',1
*cfclos

finish

/clear
/prep7
parres

*enddo


!-----------------------------------------------------------
finish
/clear

/CWD,C:\byron\ANSYS\t8w80varyLdg
/psearch,C:\byron\ANSYS\Macros
/nerr,0,,,,0

/prep7

!Dimensions----------------------
t=.8e-6
Ldw=2

n=25
!------------
g_min=2e-6
```

```
g_max=8e-6

n_g=n  !# gaps to try
*DIM,g,ARRAY,n_g                    ! init Length array
g_inc=(g_max-g_min)/(n_g-1)
*VFILL,g(1),RAMP,g_max,-g_inc       ! fill gap from g_min to g_max

!------------
L_max=300e-6
L_min=60e-6

n_L=n  !# lengths to try
*DIM,L,ARRAY,n_L                    ! init Length array
L_inc=(L_max-L_min)/(n_L-1)
*VFILL,L(1),RAMP,L_min,L_inc       ! fill L from L_min to L_max

!----------
*DIM,Ldg,ARRAY,n
*DIM,w,ARRAY,n
*do,iw,1,n
w(iw)=L(iw)/Ldw
Ldg(iw)=L(iw)/g(iw)
*enddo

*cfopen,dim,txt
write,t
write,Ldw
writer1,'g',1
writer1,'w',1
writer1,'L',1
writer1,'Ldg',1
*cfclos


*do,iLdg,1,n
parsav,all

c_c_qtr_pl_br,w(iLdg),L(iLdg),t,g(iLdg)

*cfopen,k_s,txt,,append
write,k_stiff
*cfclos

*cfopen,f_n,txt,,append
writer1,'fn',1
*cfclos
```

```
finish

/clear
/prep7
parres


%macro for static and modal calculations

!!!!!!! READ IN GEOMETRY PARAMETERS !!!!!!!!
!!!!!!!!!!!!!!!!!!!!!!!!!!!!!!!!!!!!!!!!!!!!

b_width=arg1
b_length=arg2
b_thick=arg3
gap=arg4

T_width=2e-6
anch=8e-6

lsize_mem=b_thick               !element size for membrane

!!! DEFINE ELEMENT TYPES !!!
!!!!!!!!!!!!!!!!!!!!!!!!!!!!

et,1,SOLID45            !element type


!!! INPUT MATERIAL PROPERTIES !!!
!!!!!!!!!!!!!!!!!!!!!!!!!!!!!!!!


mp,ex,1,70e9            !Young's modulus of structural material 1 (aluminum membrane)
mp,prxy,1,.34           !poison's ration of structural material 1
mp,dens,1,2700          !density of structural material 1


!!! CREATE GEOMETRY !!!
!!!!!!!!!!!!!!!!!!!!!!!
numstr,volu,1

BLock,0,b_width/2,0,b_thick,-b_thick,b_length/2     ! Creates a rectangle  1

BLock,0,b_width/2,b_thick,-gap,0,-b_thick   ! Creates a rectangle  2
```

```
Block,0,b_width/2,-gap,-gap+b_thick,0,-b_thick-anch         ! Creates a rectangle  3

vovlapk,1,2,3


/ANGLE, 1 ,60.000000,YS,1 ! Rotates the display
/REPLOT,FAST                          ! Fast redisplay


esize,lsize_mem                       ! Element size
!mshape,1,3D                !use quads, not triangles
vmesh,all                       ! Mesh the volume
allsel,all


!!!!! APPLY STRUCTURAL BCS AND LOADING !!!!!!
!!!!!!!!!!!!!!!!!!!!!!!!!!!!!!!!!!!!!!!!!!!!!!!
ASEL,S,LOC,y,-gap                     ! Area select at z=0
DA,All,ALL,0                ! Constrain the area
ASEL,ALL                    ! Reselect all areas

ASEL,S,LOC,Z,b_length/2                       ! Area select at z=b_length/2
DA,all,Symm                 ! Constrain the area
ASEL,ALL                    ! Reselect all areas

ASEL,S,LOC,X,b_width/2                        ! Area select at z=b_length/2
dA,all,Symm                 ! Constrain the area
ASEL,ALL                    ! Reselect all areas


!!!!! ENTER SOLUTION !!!!!!
!!!!!!!!!!!!!!!!!!!!!!!!!!!

/SOLU
antype,static,new

Nn=Node(b_width/2,b_thick,b_length/2)

n_l=4                   !# of loading steps
*DIM,P,ARRAY,n_l                ! dimension 1 x n numeric array
*VFILL,P(1),RAMP,10e-5,10e-4/(n_l-1)       ! fill vector 2 with values starting at 0 and
inc by 10
*DIM,F_y,ARRAY,n_l
*DIM,d,ARRAY,n_l
```

```
*do,i,1,n_l

KSEL,S,LOC,Z,b_length/2              ! Select certain keypoint
KSEL,R,LOC,Y,b_thick
KSEL,R,LOC,X,b_width/2
FK,All,FY,P(i)                       ! Force on keypoint
KSEL,ALL                        ! Reselect all keypoints

solve

*get,disp_y,node,Nn,U,y
d(i)=disp_y
F_y(i)=4*P(i)

*enddo

finish

/solu                   !enter solution processor

antype,modal,new        !select a new harmonic analysis
MODOPT,LANB,2

MXPAND,2
solve

finish

*DIM,fn,ARRAY,2
*do,q,1,2
*get,f,mode,q,freq
fn(q)=f
*enddo

lin_reg,'d','F_y'

k_stiff=a1
```

APPENDIX B:

EIGENVALUE AND MODESHAPE CALCULATION

```
function[lm2]=lm_R(Ldw,Ldg,poissons)
k=15;
%n=10;
%n2=5;
%phi=linspace(.33,1,n);  % w/L
%Kr=-linspace(10,150,n2);          % L/g
phi=1./Ldw;
Kr=-Ldg;
lm_g=5.52;
w=4;

options = optimset(@fminbnd); options.MaxFunEvals=1e5; options.MaxIter=1e5; options.TolFun=1e-50;  options.TolX=1e-50;
for i=1:length(Ldg);
      [lm,FVAL,EXITFLAG,OUTPUT] = fminbnd(@Eigmat,lm_g-w,lm_g+w,options,phi(i),k,Kr(i),poissons);
      lm2(i,1)=lm*4;
end


function [dt]=Eigmat(lm,phi,k,Kr,v)
vi=2-v;
ak=k;
k1=2*k-1;
j2=2*k;
phis=phi*phi;

for m=1:j2;
   for n=1:j2;
      A(m,n)=0;
   end
end
for m=1:2:k1;
   for n=0:1:k-1;%1:2:k1;
      i=(m+1)/2;
      j=(n+1);%/2;
      enp=n*pi;
      enps=enp*enp;
      emp=m*pi/2;
      emps=emp*emp;
      bms=phis*(lm+emps);
      bm=sqrt(bms);
```

```
      x1=lm-emps;
      if x1<=0;
         gms=-phis*x1;
         gm=sqrt(gms);
         phi2m=bm*(vi*phis*emps-bms)*sinh(bm)/(gm*(gms-vi*phis*emps)*sinh(gm));
         phi22m=(v*phis*emps-bms)*cosh(bm)+phi2m*(v*phis*emps-gms)*cosh(gm);
         if n==0;
            A(i,i)=1; % 1,1  %-1/(bm+gm);

A(j+k,i)=((bm*sinh(bm)/(bms+enps))+phi2m*gm*(sinh(gm)/(gms+enps)))*emp*cos(en
p)/phi22m; % 3,1 %-2*emp*enp/((gms+enps)*(bms+enps));
         else

A(j+k,i)=2*((bm*sinh(bm)/(bms+enps))+phi2m*gm*(sinh(gm)/(gms+enps)))*emp*cos(
enp)/phi22m; % 3,1 %-2*emp*enp/((gms+enps)*(bms+enps));
         end
      else
         gms=phis*x1;
         gm=sqrt(gms);
         phi1m=bm*(vi*phis*emps-bms)*sinh(bm)/(gm*(vi*phis*emps+gms)*sin(gm));
         phi11m=(v*phis*emps-bms)*cosh(bm)+phi1m*(v*phis*emps+gms)*cos(gm);
         if n==0;
            A(i,i)=1;              %                    1,1                    %-
(gm*sin(gm)+bm*cos(gm)*sinh(bm)/cosh(bm))/(cos(gm)*(gms+bms));
            A(j+k,i)=((bm*sinh(bm)/(bms+enps))+phi1m*gm*(sin(gm)/(gms-
enps)))*emp*cos(enp)/phi11m;  % 3,1  %2*emp*enp/((gms-enps)*(bms+enps));
         else
            A(j+k,i)=2*((bm*sinh(bm)/(bms+enps))+phi1m*gm*(sin(gm)/(gms-
enps)))*emp*cos(enp)/phi11m;  % 3,1  %2*emp*enp/((gms-enps)*(bms+enps));
         end
      end
   end
end
for m=1:2:k1;
   for n=0:1:k-1; %1:2:k1;
      i=(m+1)/2;
      j=(n+1); %/2;
      enp=n*pi;
      enps=enp*enp;
      emp=m*pi/2;
      emps=emp*emp;
      bns=(enps+lm*phis)/phis;
      bn=sqrt(bns);
      x1=lm*phis-enps;
      if x1<0;
         gns=-x1/phis;
```

```
        gn=sqrt(gns);
        x11=(enps-v*phis*gns)/(gns+emps)-(enps-v*phis*bns)/(bns+emps);
        if m>1;
           A(i,j+k)=2*emp*cos(enp)*(x11/(gns-bns));%          1,3          %-
2*enp*emp/((gns+emps)*(bns+emps)); -  ?
        else
           A(j+k,j+k)=(bn*cosh(gn)*sinh(bn)-gn*cosh(bn)*sinh(gn))/((gns-
bns)*cosh(bn)*cosh(gn))+1/Kr; % 3,3   -1/(bn+gn);
           A(i,j+k)=2*emp*cos(enp)*(x11/(gns-bns));%          1,3          %-
2*enp*emp/((gns+emps)*(bns+emps));  %1,3 -
        end
      else
        gns=x1/phis;
        gn=sqrt(gns);
        x11=(enps+v*phis*gns)/(gns-emps)+(enps-v*phis*bns)/(bns+emps);
        if m>1;
           A(i,j+k)=2*emp*cos(enp)*(x11/(gns+bns));%    1,3        %2*enp*emp/((gns-
emps)*(bns+emps));%-  ?
        else
           A(j+k,j+k)=-
(gn*sin(gn)*cosh(bn)+bn*cos(gn)*sinh(bn))/((gns+bns)*cosh(bn)*cos(gn))+1/Kr; %  3,3
%-(gn*sin(gn)+bn*cos(gn)*sinh(bn)/cosh(bn))/(cos(gn)*(gns+bns));%-  ?
           A(i,j+k)=2*emp*cos(enp)*(x11/(gns+bns));%    1,3        %2*enp*emp/((gns-
emps)*(bns+emps));%-  ?
        end
      end
   end
end
A;
dt= abs(det(A));



is=2*k-1;
for m=1:is;
   for n=1:is;
      BB(m,n)=A(m,n+1);
   end
end
for m=1:is;
   B1(m)=-A(m,1);
end

B1=BB\B1'
EM(1)=1;
EN(1)=B1(k);
```

```
for L=2:k;
   EN(L)=B1(k+L-1);
   EM(L)=B1(L-1);
end

for L=1:k;

end
k1=k1-2;
nxx=50;
for n=1:nxx
   for m=1:nxx
      W(n,m)=0;
   end
end
for L=1:nxx;
   psi=(L-1)/(nxx-1);
   for J=1:nxx;
      eta=(J-1)/(nxx-1);

for m=1:2:k1;
   mm=(m+1)/2;

   emp=m*pi/2;
   emps=emp*emp;
   bms=phis*(lm+emps);
   bm=sqrt(bms);
   x1=lm-emps;
   if x1<=0;
      gms=-phis*x1;
      gm=sqrt(gms);

      phi2m=bm*(vi*phis*emps-bms)*sinh(bm)/(gm*(gms-vi*phis*emps)*sinh(gm));
      phi22m=(v*phis*emps-bms)*cosh(bm)+phi2m*(v*phis*emps-gms)*cosh(gm);


W(L,J)=W(L,J)+EM(mm)/phi22m*(cosh(bm*eta)+phi2m*cosh(gm*eta))*sin(emp*psi);
   else
      gms=phis*x1;
      gm=sqrt(gms);
      phi1m=bm*(vi*phis*emps-bms)*sinh(bm)/(gm*(vi*phis*emps+gms)*sin(gm));
      phi11m=(v*phis*emps-bms)*cosh(bm)+phi1m*(v*phis*emps+gms)*cos(gm);


W(L,J)=W(L,J)+EM(mm)/phi11m*(cosh(bm*eta)+phi1m*cos(gm*eta))*sin(emp*psi);
   end
```

```
end

for n=0:1:k-1; %1:2:k1;
   nn=(n+1); %/2;
   enp=n*pi;
   enps=enp*enp;
   bns=(enps+lm*phis)/phis;
   bn=sqrt(bns);
   x1=lm*phis-enps;
   if x1<0;
      gns=-x1/phis;
      gn=sqrt(gns);
      %x11=(enps-v*phis*gns)/(gns+emps)-(enps-v*phis*bns)/(bns+emps);
      W(L,J)=W(L,J)-EN(nn)/((gns-bns)*cosh(gn))*(cosh(gn*(1-psi))-
cosh(gn)/cosh(bn)*cosh(bn*(1-psi)))*cos(enp*eta);
   else
      gns=x1/phis;
      gn=sqrt(gns);
      %x11=(enps+v*phis*gns)/(gns-emps)+(enps-v*phis*bns)/(bns+emps);
      W(L,J)=W(L,J)+EN(nn)/((gns+bns)*cos(gn))*(cos(gn*(1-psi))-
cos(gn)/cosh(bn)*cosh(bn*(1-psi)))*cos(enp*eta);
   end
end
end
end
psi=linspace(0,1,nxx);
eta=linspace(0,1,nxx);
surf(psi,eta,W)
```

REFERENCES

1. Binnig, G., C.F. Quate, and C. Gerber, *Atomic force microscope.* Physical Review Letters, 1986. **56**(9): p. 930-3.

2. Cappella, B. and G. Dietler, *Force-distance curves by atomic force microscopy.* Surface Science Reports, 1999. **34**(1-3): p. 1-4.

3. Cappella, B., H.J. Butt, and M. Kappl, *Force measurements with the atomic force microscope: Technique, interpretation and applications.* Surface Science Reports, 2005. **59**(1-6): p. 1-152.

4. Degertekin, F.L., et al., *Sensor for direct measurement of interaction forces in probe microscopy.* Applied Physics Letters, 2005. **87**(21): p. 213109-1.

5. Tortonese, M., R.C. Barrett, and C.F. Quate, *Atomic resolution with an atomic force microscope using piezoresistive detection.* Applied Physics Letters, 1993. **62**(8): p. 834-6.

6. Meyer, G. and N.M. Amer, *Novel optical approach to atomic force microscopy.* Applied Physics Letters, 1988. **53**(12): p. 1045-7.

7. Schonenberger, C. and S.F. Alvarado, *A differential interferometer for force microscopy.* Review of Scientific Instruments, 1989. **60**(10): p. 3131-4.

8. Martin, Y., D.W. Abraham, and H.K. Wickramasinghe, *High-resolution capacitance measurement and potentiometry by force microscopy.* Applied Physics Letters, 1988. **52**(13): p. 1103-5.

9. Sarid, D., et al., *Compact scanning-force microscope using a laser diode.* Optics Letters, 1988. **13**(12): p. 1057-9.

10. Onaran, A.G., et al., *A new atomic force microscope probe with force sensing integrated readout and active tip.* Review of Scientific Instruments, 2006. **77**(2): p. 23501-1.

11. Hall, N. and F.L. Degertekin. *An integrated optical detection method for capacitive micromachined ultrasonic transducers*. 2000. San Juan, Puerto Rico: IEEE.

12. Hall, N.A. and F.L. Degertekin, *Integrated optical interferometric detection method for micromachined capacitive acoustic transducers.* Applied Physics Letters, 2002. **80**(20): p. 3859.

13. Solgaard, O., F.S.A. Sandejas, and D.M. Bloom, *Deformable grating optical modulator.* Optics Letters, 1992. **17**(9): p. 688-90.

14. Sulchek, T., et al., *Parallel atomic force microscopy with optical interferometric detection.* Applied Physics Letters, 2001. **78**(12): p. 1787.

15. Hall, N.A., *Ph.D. Thesis in Mechanical Engineering*. 2004, Georgia Institute of Technology: Atlanta, GA.

16. Gere, J.M., *Mechanics of Materials*. 2001, Pacific Grove, CA Brooks/Cole.

17. Blevins, R.D., *Formulas for natural frequency and mode shape*. 1995, Malabar, FL.: R.E. Krieger.

18. Gorman, D.J.D.J., *Free vibration analysis of rectangular plates*. 1981, New York, NY.: Elsevier.

19. Senturia, S.D., *Microsystem Design*. 2001, Boston, MA.: Kluwer Academic Publishers.

20. Huang, J.M., et al., *Mechanical design and optimization of capacitive micromachined switch.* Sensors and Actuators, A: Physical, 2001. **93**(3): p. 273-285.

21. Soedel, W., *Vibrations of shells and plates*. Vol. 3rd ed. 2001, New York, NY.: Marcel Dekker.